



**HAL**  
open science

# A new method to evaluate the power ratio distributions of astronomical signals: A case study from Upper Cretaceous terrestrial sediments

He Huang, Hanting Zhong, Chao Ma, Matthias Sinnesael, Yuan Gao, Yuyin  
Li, Mingcai Hou, Chengshan Wang

## ► To cite this version:

He Huang, Hanting Zhong, Chao Ma, Matthias Sinnesael, Yuan Gao, et al.. A new method to evaluate the power ratio distributions of astronomical signals: A case study from Upper Cretaceous terrestrial sediments. *Geological Society of America Bulletin*, In press, 10.1130/B37208.1 . hal-04449122

**HAL Id: hal-04449122**

**<https://hal.science/hal-04449122>**

Submitted on 19 Feb 2024

**HAL** is a multi-disciplinary open access archive for the deposit and dissemination of scientific research documents, whether they are published or not. The documents may come from teaching and research institutions in France or abroad, or from public or private research centers.

L'archive ouverte pluridisciplinaire **HAL**, est destinée au dépôt et à la diffusion de documents scientifiques de niveau recherche, publiés ou non, émanant des établissements d'enseignement et de recherche français ou étrangers, des laboratoires publics ou privés.

1 **A new method to evaluate the power ratio distributions of astronomical**  
2 **signals: a case study from Upper Cretaceous terrestrial sediments**

3 He Huang<sup>1,2,3</sup>, Hanting Zhong<sup>1,2,\*</sup>, Chao Ma<sup>1,2</sup>, Matthias Sinnesael<sup>3</sup>, Yuan Gao<sup>4</sup>, Yuyin Li<sup>1,2</sup>,  
4 Mingcai Hou<sup>1,2</sup>, Chengshan Wang<sup>4</sup>

5 <sup>1</sup> *Key Laboratory of Deep-time Geography and Environment Reconstruction and Applications of Ministry of*  
6 *Natural Resources, Chengdu University of Technology, Chengdu 610059, China*

7 <sup>2</sup> *State Key Laboratory of Oil and Gas Reservoir Geology and Exploitation, Institute of Sedimentary Geology,*  
8 *Chengdu University of Technology, Chengdu 610059, China*

9 <sup>3</sup> *IMCCE, CNRS, Observatoire de Paris, PSL University, Sorbonne Université, 75014, Paris, France*

10 <sup>4</sup> *State Key Laboratory of Biogeology and Environmental Geology, China University of Geosciences (Beijing),*  
11 *Beijing 100083, China*

12 \*Corresponding author (e-mail: [zhonghanting@cdut.edu.cn](mailto:zhonghanting@cdut.edu.cn))

13 **ABSTRACT**

14 Astronomical cycles reliably identified in the sedimentary record are useful for their  
15 paleoclimatic interpretations and construction of astrochronology. However, the depositional  
16 response and burial-diagenesis processes play a crucial role in distorting the time scales of  
17 geological records and introducing noise to orbital signals. How to evaluate the response of  
18 varied depositional environments to astronomical forcing remains a challenge. We developed the  
19 random-length average orbital power ratio calculation (RAOPR) method to evaluate average  
20 orbital power ratio distributions within a specific time interval and applied this new method to  
21 the theoretical eccentricity–tilt–precession (ETP) plus noise series and an astronomically tuned  
22 Cretaceous terrestrial stratigraphic record spanning ~24 m.y. (92–65 Ma, except for an ~3.8 m.y.  
23 gap from ca. 79.9 Ma to 76.1 Ma). Using the merged ETP plus noise series, we observed

24 different orbital power ratio distributions for different background noise intervals. For the  
25 Cretaceous terrestrial Songliao Basin, we retrieved long-term orbital variations and used the  
26 RAOPR method to calculate the average orbital power ratios in different depositional  
27 environment intervals. Our results suggest that unusually high precession power in the Yaojia  
28 Formation resulted, in part, from autogenic processes, and unusually low precession power in the  
29 Nenjiang Formation can be attributed to marine incursion events. The eccentricity power of the  
30 meandering river facies was much higher than observed in other facies intervals. Conversely, the  
31 lowest precession power in the meandering facies may be attributed, in part, to the erosion  
32 “clipping” effect, which decreases the high-frequency precession band power and increases  
33 low-frequency eccentricity band power.

34 **Key words:** Orbital cycles; paleoclimate proxies; depositional processes; RAOPR; Songliao  
35 Basin

## 36 1. INTRODUCTION

37 Sedimentary archives contain complex signals produced by multiple climatic and  
38 depositional processes. These signals can include cyclical astronomical signals (i.e.,  
39 Milankovitch cycles), irregular oscillations and abrupt events (Hinnov, 2013; Li et al., 2019b;  
40 Meyers, 2019). The astronomical cycles have been widely identified in stratigraphic time series  
41 by state-of-art spectral analysis tools (Meyers et al., 2014; Li et al., 2019a), which greatly  
42 improved the fidelity of cyclostratigraphy. Therefore, in recent year, multiple indirect proxies  
43 with climate-induced signatures in sediments have been proposed for reconstructing  
44 paleoclimate and establishing astronomical time scales (ATS) (e.g., Hays et al., 1976; Hinnov,

45 2013; Westerhold et al., 2020). However, these orbital signals are often affected by  
46 heterogeneous depositional processes, burial-diagenesis processes and stochastic noise (Meyers,  
47 2012; Sinnesael et al., 2018; Li et al., 2019b; Meyers, 2019; Wouters et al., 2022), and all of  
48 these depositional factors make the interpretation of sedimentary signals sometimes challenging.  
49 Among them, the depositional response and burial-diagenesis processes are particularly  
50 significant as they contribute to the distortion of geological record time scales and introduce  
51 noise into orbital signals (Meyers, 2019). However, there remains a lack of research in this  
52 specific area.

53 Terrestrial sedimentary environments present a unique challenge compared to marine  
54 depositional settings due to the superimposition of local climatic information and distinct  
55 depositional processes that vary from place to place. Some simulation works have emphasized  
56 the terrestrial depositional processes could transform the orbital signals before they preserved  
57 (e.g., Sadler and Strauss., 1990; Bazykin et al., 1997; Hajek and Straub, 2017; Wang Y et al.,  
58 2023). Therefore, it seems that the changing climate backgrounds and/or depositional processes  
59 may have different impacts on recording consistent external orbital signals. For instance, in an  
60 alluvial river system, channel avulsion is a typical autogenic phenomenon, and the stratigraphic  
61 record of this process may exhibit periodic-like variations (e.g., Willwood Formation, Abels et  
62 al., 2013). Therefore, caution must be exercised in interpreting cyclic environmental signals in  
63 alluvial sedimentary successions, and various methods should be utilized (for instance the  
64 average spectral misfit (ASM, Meyers and Sageman, 2007), time scale optimization (TimeOpt,  
65 Meyers, 2015), evolutionary time scale optimization (eTimeOpt, Meyers, 2015, 2019),  
66 correlation coefficient (COCO & eCOCO, Li et al., 2018)), where necessary, to ascertain the  
67 reliability of such periodic signals. In addition to the fluvial system, delta and shallow lake

68 depositional settings may also be affected by the dynamics of the source-to-sink network (Carroll  
69 and Bohacs, 1999; Allen, 2008). Variations in the sediment transport system can give rise to  
70 episodes of sediment storage and release, which have the potential to impart rhythmic features to  
71 the stratigraphic record. These autogenic depositional processes (e.g., delta growth, shoreline  
72 progradation) can generate not only periodic signals (noise) but also obscure some genuine  
73 climate signals prior to their incorporation into the sedimentary archive (Kim et al., 2010).  
74 Moreover, variations in accommodation are associated with the dynamics of the equilibrium  
75 profile and all allogenic processes (tectonics of source area, basin subsidence, climate, and lake  
76 level fluctuation) (e.g., Huang et al., 2021a), which are intrinsically combined with autogenic  
77 processes and impact the preservation of orbital signals in the stratigraphic record (Hinnov,  
78 2000).

79 To some extent, recent studies have examined the impact of depositional processes on the  
80 preservation of orbital signals within strata, with investigations conducted in both marine  
81 environments (Li et al., 2019a; Levy et al., 2019) and terrestrial lake settings (Wang Z et al.,  
82 2021; Walters et al., 2023; Wang Y et al., 2023). However, comprehending the complete picture  
83 behind this scene, particularly within complex terrestrial sedimentary systems, remains  
84 challenging. The evaluation of astronomical signal features in different depositional backgrounds  
85 poses two fundamental challenges: the need for a proper evaluation method to decipher these  
86 coded messages and a long, continuous geological record that covers different depositional  
87 environments. Therefore, the main objectives of this study are to: 1) develop a new evaluation  
88 method (i.e., *Random-length average orbital power ratio calculation*, RAOPR) for assessing  
89 different depositional settings response to astronomical forcing; 2) evaluate the orbital power  
90 distributions in diverse depositional backgrounds within the astronomically-tuned terrestrial

91 record obtained from the SK-1 core in the SLB; 3) ascertain the influences of depositional  
92 processes on preserving the orbital signals in the Late Cretaceous SLB.

## 93 **2. GEOLOGICAL SETTING**

### 94 **2.1 Geological background of the Songliao Basin and the SK-1 drilling core**

95 The SLB covers roughly 260,000 km<sup>2</sup> in Heilongjiang, Jilin, and Liaoning provinces of NE  
96 China (Fig. 1A). During the Cretaceous, the SLB was a large rift basin and preserved as much as  
97 10,000 m of sediments with volcanoclastic, alluvial fan, fluvial and lacustrine facies (Wang C et  
98 al., 2013). The first phase of the International Continental Scientific Drilling Project (SK-1)  
99 obtained a total of 2486 m of composite core, combining the south core (SK-1s) and the north  
100 core (SK-1n) (Fig. 1B). In the ascending order, the SK-1 core contains the Quantou (K<sub>2</sub>q),  
101 Qingshankou (K<sub>2</sub>qn), Yaojia (K<sub>2</sub>y), Nenjiang (K<sub>2</sub>n), Sifangtai (K<sub>2</sub>s) and Mingshui (K<sub>2</sub>m)  
102 Formations (Fig. 2). Due to the relative short duration of the Quantou Formation in the SK-1s  
103 core, this formation was excluded for performing the RAOPR analysis in this study.

104 In the SK-1 core, the Qingshankou Formation consists of dark gray and black mudstone  
105 interbedded with oil shale, indicating a deep lacustrine (DL) depositional environment (Feng et  
106 al., 2010; Wang C et al., 2013). The Yaojia Formation comprises red, gray, grayish green  
107 mudstone, siltstone and sandstone, which deposited in a shallow lake (SL) setting (Feng et al.,  
108 2010; Wang C et al., 2013). The first and second members of Nenjiang Formation (K<sub>2</sub>n<sub>1</sub>- K<sub>2</sub>n<sub>2</sub>)  
109 are dominated by gray to black mudstone, marl, shelly limestone, and oil shale interbedded with  
110 gray siltstone and fine sandstone, which deposited in a deep lake (DL) environment (Feng et al.,  
111 2010; Wang C et al., 2013). The third to fifth members of Nenjiang Formation consist of grey,

112 red, grayish mudstone, siltstone and sandstone, reflecting a delta to meandering river facies  
113 (DEL-MR) (Feng et al., 2010; Wang C et al., 2013). The Sifangtai Formation consists of  
114 brick-red pebbly sandstone and shale interbedded with brown, gray and gray-green sandstone  
115 and muddy siltstone (Feng et al., 2010; Wang C et al., 2013). The Mingshui Formation is  
116 composed of gray-green, gray, black and brown-red shale and gray-green sandstone (Feng et al.,  
117 2010; Wang C et al., 2013). The lithological associations in the Sifangtai and Mingshui  
118 formations indicate a meandering river (MR) facies (Feng et al., 2010; Wang C et al., 2013). We  
119 also noticed that in the Sifangtai and Mingshui Formations, four episodes of shallow lake facies  
120 were identified (Table. S2) (Wang C et al., 2013), while these four short duration (~1 Myr) SL  
121 facies intervals would not have a significant impact on subsequent average power ratios  
122 calculations.

## 123 **2.2 Age framework of the SK-1 drilling core**

124 The chronostratigraphic framework of the SK-I composited core is constrained by  
125 biostratigraphy (Wan et al., 2013), magnetostratigraphy (Deng et al., 2013) and high-quality  
126 CA-ID-TIMS U-Pb zircon radiometric ages (Wang T et al., 2016). Four  $^{206}\text{Pb}/^{238}\text{U}$  ages of  
127  $91.886 \pm 0.11$  Ma,  $90.974 \pm 0.12$  Ma,  $90.536 \pm 0.12$  Ma, and  $83.269 \pm 0.11$  Ma were determined  
128 (Fig. 3) (Wang T et al., 2016). Eleven local magnetozones have been identified as Chrons C34n  
129 to C28n (Fig. 3) (Deng et al., 2013). Meanwhile, an astronomical time scale was established by  
130 tuning the 405 kyr eccentricity cycles extracted from Th logging data to the La2010d target  
131 curve based on the magnetostratigraphic time framework of the SK-1n borehole (Wu et al.,  
132 2014). The initial anchor points for tuning to La2010d were selected from C30n/C29r and  
133 C34n/C33r reversal boundary, which respectively located in the K<sub>2</sub>m and K<sub>2</sub>n (Fig. 3) (Deng et

134 al., 2013; Wu et al., 2014). Recently, chronostratigraphic framework of the SK-1s core has been  
135 revised by cyclostratigraphic analysis of the Th series, which provides a continuous geological  
136 time framework from 92.531 Ma to 82.358 Ma (Wu et al., 2022). In this study, we adopt the new  
137 high-precision radio-isotopically constrained ATS for the SK-1s core, because this new age  
138 model has greatly improved the time framework of the Nenjiang Formation, while the SK-1n  
139 core age model is still adopted from Th-calibrated ATS in Wu et al (2014). Therefore, the  
140 ATS-calibrated boundary ages for various layers in the SK-1n and SK-1s cores were determined  
141 (Table. S2), revealing an ~3.8 Myr-long hiatus between the K<sub>2n</sub> and K<sub>2s</sub> in the SK-1n core from  
142 79.9 to 76.1 million years ago.

### 143 **2.3 Paleoclimate proxy**

144 Milankovitch signals can be recorded in the strata through periodic climatic shifts and  
145 associated depositional feedbacks, such as changes in precipitation and temperature, monsoon  
146 intensity, weathering and runoff rates. Multiple paleoclimate proxies, including gamma ray (GR),  
147 thorium (Th), density (Den), XRF, total organic carbon content (TOC) and organic carbon  
148 isotope ( $\delta^{13}\text{C}_{\text{org}}$ ) have been used to recognize the Milankovitch cycles through objective  
149 statistical analysis (e.g., average spectral misfit (ASM, Meyers and Sageman, 2007), time scale  
150 optimization (TimeOpt, Meyers, 2015), evolutionary time scale optimization (eTimeOpt, Meyers,  
151 2015, 2019), correlation coefficient (COCO & eCOCO, Li et al., 2018)) in the SLB (Wu et al.,  
152 2013, 2014; Huang et al., 2021a; Zhang et al., 2022; Li et al., 2022). However, only the thorium  
153 (Th) logging data has been tuned for establishing the ATS of the SK-1 composite core, obviating  
154 the necessity for reconducted astronomical tuning by ourselves. Therefore, the  
155 astronomically-tuned Th time series has covered different types of depositional environment

156 intervals (Wu et al., 2014; 2022). Moreover, the Th values are closely associated with the  
157 lithological changes and can reflect the paleoclimate features, such as precipitation, weathering  
158 and terrestrial inputs (Wu et al., 2014; 2022; Li et al., 2019b; Zhang et al., 2022). In this study,  
159 the Th well logging data was used as the paleoclimatic and paleoenvironmental proxy for  
160 evaluation of the orbital signal distributions in different depositional environment intervals in the  
161 Songliao Basin.

## 162 **3. METHODOLOGY**

### 163 **3.1 Spectral analysis**

164 The multi-taper method (MTM; Thomson, 1982) with a red noise null hypothesis model  
165 (Mann and Lees, 1996) and the wavelet spectral analysis (Torrence and Compo, 1998) were  
166 applied for seeking the orbital signals in the detrended Th time series (data from Wu et al., 2014,  
167 2022) (Fig. 4). Prior to spectral analysis, the astronomically-tuned Th series was firstly linear  
168 interpolated to the medium sampling rate (~1.43 kyr) to obtain an even time series. The long  
169 eccentricity signals were extracted from the stratigraphic series using a Gaussian bandpass filter  
170 with a bandwidth at 0.002-0.003 kyr<sup>-1</sup> (Fig. 4). All of these spectral analysis were performed in  
171 the *Acycle* software (Li et al., 2019a).

### 172 **3.2 Calculation of the orbital power variations**

173 To date, there have been only a limited number of studies that have utilized statistical  
174 methods to compute the power and band power ratios of climate proxy data in the time domain  
175 (e.g., Meyers, 2012; Li et al., 2016; Ma et al., 2017; 2019; Huang et al., 2020). The

176 *integratePower* algorithm determines the total power within a given bandwidth, and also the  
177 ratio of this power to the total power in the spectrum (Meyers et al., 2014). Similarly, Li et al  
178 (2019b) introduced a power decomposition analysis (PDA) method to calculate and compare  
179 dynamic target orbital power to total power ratio of multiple proxies from the same time and  
180 locality, so as to test their sensitivities to external climate forcing. Recently, a sedimentary noise  
181 model (DYNOT) was proposed to reconstruct past sea-level changes based on the ratio of signal  
182 variance unrelated to orbital forcing in paleoclimate proxies (i.e., noise) to the total variance in  
183 proxies (Li et al., 2018a). Afterwards, many studies have demonstrated that this model can be  
184 applied to also infer paleolake level changes (e.g., Wang et al., 2020; Huang et al., 2020; Zhang  
185 et al., 2022; Wei et al., 2023), finding that the DYNOT ratio was lower during lake level  
186 high-stands than during intervals of low lake level. Hence, these statistical methods can be  
187 employed in the evaluation of orbital/noise power variations in astronomical-tuned time series  
188 (Fig. 5).

189 Here, we employ the PDA, *integratePower* and DYNOT methods to assess the orbital  
190 signal power variations in both the theoretical eccentricity-tilt-precession (ETP) (Laskar et al.,  
191 2004) and the synthetic ETP-plus-noise time series (with a length of 10000 kyr and temporal  
192 resolution of 1 kyr) (Fig. 5). We only investigate the frequencies and their power lower than 0.08  
193 kyr<sup>-1</sup> (12.5 kyr/cycle), because all of the astronomical signal frequencies (precession, obliquity  
194 and eccentricity) are located at this range. Four intervals with different types of noise have been  
195 incorporated into the theoretical ETP series (Fig. 5d) (modified from Li et al., 2018). All of these  
196 ETP+noise series are generated from *Acycle* software (Li et al., 2019a).

### 197 **3.3 Random-length Average Orbital Power Ratio calculation (RAOPR)**

#### 198 **3.3.1 Motivation for developing the RAOPR method**

199 Although the PDA, *integratePower*, and DYNOT methods offer a semi-quantitative  
200 approach to assessing the orbital signals power variations, the inherent long-term orbital signal  
201 power variations still exist (Fig. 5). Therefore, distinguishing between the inherent long-term  
202 cycles and changes in orbital signal strength resulting from different climatic backgrounds or  
203 depositional processes remains challenging. The inherent long-term orbital signals mainly  
204 include the ~2.4-Myr eccentricity and ~1.2-Myr obliquity cycles during the Cretaceous period  
205 (Laskar et al., 2004; Ma et al., 2017, 2019; Wu et al., 2022). Nonetheless, in the Triassic period,  
206 the eccentricity amplitude modulation (AM) cycle appears to be shorter (Olsen et al., 2019).  
207 Levy et al. (2019) applied the *integratePower* algorithm to compute the obliquity sensitivity by  
208 dividing obliquity variance (i.e., 1.2-Myr amplitude modulation cycle) in a compiled  $\delta^{18}\text{O}$   
209 mega-splice (from ~5-34 Ma) by the variance of the theoretical obliquity solution, which  
210 effectively eliminating the inherent 1.2-Myr long-term obliquity variation. However, due to the  
211 inherent limitation of the astronomical solutions and the age precision of the sedimentary  
212 successions, this process is only viable within the last 55 Ma (Laskar et al., 2004). Thus, to  
213 address these shortages, we develop a new method (RAOPR) for assessing orbital power  
214 variations in regarding to compare the orbital signal patterns in different climate and/or  
215 depositional backgrounds.

#### 216 **3.3.2 The RAOPR method**

217 The *integratePower* algorithm, in its original form, employs power ratios to quantify the

218 contribution of the isolated orbital power to the total power, which equals to the isolated band  
219 power in a defined frequency range divided to the total power of the power spectrum. This  
220 process can partly reduce the long-term amplitude modulation signal variation components of the  
221 orbital signal (e.g., Levy et al., 2019). Thus, the power ratios may have a potential usage for  
222 evaluating the orbital response sensitivity in diverse sedimentary environments, if we can  
223 remove the inherent long-term cycle imprints originated from the theoretical astronomical  
224 solutions. However, the direct subtraction of long-term cycles (i.e., ~1.2 Myr and ~2.4 Myr in  
225 the Cretaceous period) from geological records is not feasible, given the phase distortion of the  
226 orbital signal (which arises from age uncertainty, stratigraphic warping, and the lag time of  
227 depositional response) and the precision limitations of the orbital solutions (as noted by Laskar et  
228 al., 2004). Therefore, to compare the orbital power ratios and deviations at different intervals,  
229 one can average the long-term variation for a given stratigraphic succession. By repeatedly  
230 calculating the average power ratios for varying lengths of the dataset, it is possible to obtain the  
231 most probable distribution patterns of the orbital signals in a specific stratigraphic unit. This  
232 method is so-called random-length average orbital power ratio calculation (RAOPR) method,  
233 and is in its current form designed to be used in the time domain.

234 To evaluate the possible usage of the RAOPR method to reflect the orbital response  
235 sensitivity, we generated sixteen time series (with a length of 20000 kyr and temporal resolution  
236 of 1 kyr, the data length is roughly equal to the geological data that we will test in the following  
237 work), including the theoretical eccentricity-tilt-precession (ETP weight: 1:1:-1) curve (Laskar et  
238 al., 2004) and fifteen ETP with noise series (i.e., five ETP+red noise: std=0, mean=0.5,  $\rho=0.8$ ;  
239 five ETP+white noise: std=1, mean=0; five ETP+red+white noise) in the *Acycle* software (Li et  
240 al., 2019a).

241 We conducted two additional sensitivity analyses on these generated time series: (1) we  
242 evaluated the fraction of the eccentricity (E+e), obliquity (~40 kyr) and precession (~20 kyr)  
243 variance, retrieved from the ETP and ETP plus noise series by using the *integratePower*  
244 algorithm in *astrochron* package (Meyers, 2014). The spectrum integration was conducted from  
245 0.001 to 0.012 kyr<sup>-1</sup> (1000 to 83 kyr) for eccentricity, 0.018–0.036 kyr<sup>-1</sup> (~55 to 27 kyr) for  
246 obliquity and 0.038–0.058 kyr<sup>-1</sup> (~26 to 17 kyr) for precession. All the time-frequency analyses  
247 employed three  $2\pi$  prolate data tapers, with a 500 kyr window and a 5 kyr time step. The  
248 frequency band widths of obliquity and precession were adjusted to account for the shorter  
249 cycles resulting from tidal friction effects (Laskar et al., 2004). (2) We extracted random length  
250 of the power ratio data and calculated the average ratio value distributions. Because of the  
251 amplitude modulation cycles imposed on the precession (100 kyr and 400 kyr), obliquity (173  
252 kyr and 1200 kyr) and eccentricity (2400 kyr), the minimum random length (duration) was  
253 assigned at 500 kyr for precession, 1500 kyr for obliquity, 2500 kyr for eccentricity. The  
254 maximum random length is equal to the data series length (20000 kyr) subtract the maximum  
255 duration. Then we selected the random length of the time slice from each isolated power ratio  
256 curve for 5000 times, and finally we obtained 5000 average power ratio values for each orbital  
257 signal band (Fig. S1, S2, S3). The same procedure was applied to the astronomically-tuned Th  
258 time series in the SK-1 core (Fig. S4). Moreover, we also analyzed another paleoclimatic proxy  
259 (K%) from the same drilling core to test the broader applicability of this new method (see  
260 supplemental file, Fig. S5, S6).

## 261 4. RESULTS

### 262 4.1 Orbital power variations in the synthetic ETP+noise series

263 As expected from the theory and previous case studies (e.g., Meyers, 2012; Li et al., 2019b),  
264 the orbital signal strength would decrease when the noise increases (Fig. 5). The merged  
265 ETP+noise series analyzed using the PDA and *integratePower* methods exhibit low orbital signal  
266 power values due to strong noise, as shown in Figure 5. Furthermore, the DYNOT modeling  
267 results also show coeval changes with PDA and *integratePower* results but in an anti-phase  
268 manner (Fig. 5). Hence, the PDA, *integratePower*, and DYNOT methods offer a  
269 semi-quantitative approach to assessing the orbital signals power variations.

### 270 4.2 Orbital power ratio distributions in the synthetic ETP+noise series

271 We have observed that the signal of the power ratios decrease especially between the  
272 ETP+1 and the ETP+5 noise simulations (Fig. 6; Fig. S1, S2, S3), although different types of  
273 synthetic ETP+noise series displayed different reduction patterns in their orbital signal  
274 components (Fig. 6). From the ETP+red noise results, the precession power ratios decrease faster  
275 than obliquity power ratios, and the eccentricity power ratios have the same decrease rate as the  
276 precession signal (Fig. 6, S1), a phenomenon that may originate from the eccentricity-precession  
277 modulate effects. However, in the synthetic ETP+white noise series, the eccentricity power ratios  
278 decrease faster than obliquity and precession power ratios. Especially in the precession band,  
279 their power ratios are relative stable (Fig. 6, S2), the reason was that the white noise has been  
280 included in the precession bands, which increased the precession band power. Especially in the  
281 ETP+red+white noise series, when the noise increased the obliquity and precession band power

282 ratio values were became stable (Fig. 6, S3), and compared to the ETP+red noise series, we can  
283 find the obliquity and precession signals have been greatly influenced by the white noise  
284 component.

### 285 **4.3 Orbital power variations of tuned Th time series**

286 The total power of the astronomical signal in the Th sequence of SK-1 core is greatly  
287 enhanced during the Solar system chaotic event (and the OAE3) of the Qingshankou Formation,  
288 whereas the total energy in the marine transgressive interval of the Nenjiang Formation  
289 experiences a sharp decline (Fig. 7g). In the Mingshui Formation, the total power also rises  
290 rapidly during the two humid periods (Fig. 7g). The change of the eccentricity signal energy is  
291 basically consistent with the total power energy. The possible reason is that the data itself is  
292 based on the long eccentricity tuning, and therefore the eccentricity should be the strongest  
293 periodic signal, and its proportion is the highest in most layers (Fig. 7f); moreover, according to  
294 the spectral characteristics with red noise effect (Meyers, 2012), the energy integral of the  
295 eccentricity period at low frequencies accounts for most of the total energy integral.

296 The obliquity band power and power ratio demonstrate relative stability across the entire  
297 formations and display periodic variations (Fig. 7c, d). Notably, within the Qingshankou  
298 Formation, the obliquity band power and power ratio exhibit synchronous changes, whereas the  
299 Nenjiang Formation reveals discrepancies in both amplitude and phase for the obliquity band  
300 power and power ratio.

301 The precession band power and power ratio show a coeval variation pattern throughout the  
302 whole formations (Fig. 7a, b). However, there are variations in the amplitude of the band power  
303 and power ratio between the deep lake facies of the Qingshankou and Nenjiang formations.

304 Notably, the Yaojia Formation has an exceptionally high amplitude (Fig. 7a, b). Additionally, in  
305 the SK-1n core, the Mingshui Formation displays two intervals of high amplitude for the  
306 precession band power and power ratio (Fig. 7a, b). Generally, from lake facies to river delta  
307 facies, precession power and power ratio decreases (Fig. 7a, b) while the eccentricity power and  
308 power ratio increases (Fig.7e, f), the obliquity band power and power ratio are relative stable  
309 (Fig. 7c, d).

#### 310 **4.4 Orbital power ratio distributions in different Formations of SK-1 core**

311 Based on the orbital power ratios results, we have performed the RAOPR method to extract  
312 the power ratio distribution from each depositional facies intervals and calculate the average  
313 power ratio with its standard deviation ( $2\sigma$ ) (Table. 1). For the deep lake facies, the orbital signal  
314 proportions of the Qingshankou Formation are different from the lower part of the Nenjiang  
315 Formation (Fig. 8, S4). As we noticed, the eccentricity power ratio in Qingshankou Formation  
316 ( $0.289\pm 0.004$ ) is lower than that in the first and second members of the Nenjiang Formation  
317 ( $0.41\pm 0.0092$ ). The obliquity power ratios have similar values in Qingshankou ( $0.345\pm 0.0052$ )  
318 and lower part of the Nenjiang formation ( $0.331\pm 0.0102$ ), while the precession power ratios of  
319 Qingshankou Formation ( $0.152\pm 0.0042$ ) is higher than those in the first and second members of  
320 the Nenjiang Formation ( $0.053\pm 0.0024$ ) (Fig. 8; Fig. S4).

321 The shallow lake facies of the Yaojia Formation has higher eccentricity ( $0.315\pm 0.0094$ ) and  
322 precession ( $0.226\pm 0.0072$ ) power ratios than those in the Qingshankou Formation, while the  
323 obliquity band power ratio ( $0.151\pm 0.0032$ ) was much lower compared to the Qingshankou  
324 Formation (Fig. 8; Table. 1).

325 The delta to meandering river facies of the Nenjiang Formation has a higher precession

326 power ratio ( $0.143\pm 0.018$ ) than that observed in the deep lake facies of Nenjiang Formation,  
327 while the eccentricity power ratios are comparable within these two different facies in the whole  
328 Nenjiang Formation (Fig. 8; Table. 1). However, the obliquity power ratio in the delta to  
329 meandering facies interval ( $0.187\pm 0.006$ ) was much lower than that found in the deep lake facies  
330 interval ( $0.331\pm 0.0102$ ) of the Nenjiang Formation (Fig. 8; Table. 1). The meandering river  
331 facies of the Sifangtai and Mingshui formations have the highest eccentricity power ratios  
332 ( $0.427\pm 0.0092$ ,  $0.591\pm 0.0074$ ) and relative low precession power ratios ( $0.095\pm 0.0018$ ,  
333  $0.046\pm 0.002$ ), the obliquity power ratio ( $0.271\pm 0.0078$ ) in the Sifangtai Formation higher than  
334 that in the Mingshui Formation ( $0.173\pm 0.006$ ) (Fig. 8; Table. 1).

335

## 336 **5. DISCUSSION**

### 337 **5.1 Comments on the RAOPR approach**

338 In this study, we have tested different kinds synthetic ETP+noise series. The red noise  
339 exhibits more significant intensity at lower frequencies, which roughly corresponds to the  
340 primary response of the climate system (Meyers, 2012; Sinnesael et al., 2018). White noise, on  
341 the other hand, is a random signal with uniform intensity at all frequencies, signifying that it has  
342 a relative influence on high frequency bands than low frequency bands (Meyers, 2012; Sinnesael  
343 et al., 2018) (Fig. 2). From a geological perspective, the ETP+red noise models represent a  
344 straightforward stochastic process motivated by climate and depositional system dynamics  
345 (Hasselmann, 1976; Sadler and Strauss, 1990; Meyers, 2012), while the white noise source may  
346 reflect the slower response time in Earth climatic and depositional systems (Meyers, 2012).

347 Besides, in the ETP+red noise models, the high-frequency orbital signal (e.g., precession) seems  
348 easier influenced by the sedimentary noise (Fig. 6), and this phenomenon has been observed  
349 from the geological records (Ripepe and Fischer, 1991; Meyers, 2019; Huang et al., 2020). These  
350 modeling results confirm that our assessment of the isolated average power ratios is robust for  
351 calculating the orbital response variabilities in geological records. Furthermore, this method also  
352 can normalize the secular changes in the sensitivity of sedimentation to Milankovitch-forced  
353 climate change.

354 However, the current form of this new method also exhibits certain limitations. To illustrate,  
355 firstly, it is exclusively applicable to astronomically-tuned records. Secondly, due to the presence  
356 of long-term amplitude modulation signals (e. g., 2.4 Ma eccentricity AM cycle), this method  
357 imposes stringent prerequisites on the data length. Thus, we recommend a minimum data length  
358 of 3 m.y., considering the edge effect of the *integratePower* approach.

## 359 **5.2 Orbital signal power variations from 92 Ma to 66 Ma in the SK-1 core**

360 Geological records provide an avenue for exploring the dynamics of theoretical celestial  
361 motion and the chaotic behavior of the Solar system (e.g., Ma et al., 2017, 2019; Wu et al., 2022;  
362 Olsen et al., 2019; Zeebe and Lourens, 2019). Recent studies have shown that integrated orbital  
363 power variations, specifically in the short eccentricity and obliquity band power curves, can  
364 reveal the secular resonance transition during the Late Cretaceous (Ma et al., 2017, 2019). In the  
365 Songliao Basin, the short eccentricity and obliquity band power curves in the SK-1s core  
366 (92.53-82.35 Ma) were retrieved from the astronomically-tuned Th time series and *Ostracode*  
367 shell abundance dataset to reveal the secular resonance transition during the Late Cretaceous  
368 (Wu et al., 2022).

369 The relative wide eccentricity (1/1000 kyr to 1/83 kyr frequencies bands) band power curve  
370 is generally comparable with the sole short eccentricity (~83-127 kyr) integrated band power  
371 from Wu et al (2022), in terms of both the amplitude and the pattern of secular variations from  
372 91.97 Ma to 82.35 Ma. The 2.4 Myr to 1.2 Myr and back to 2.4 Myr secular resonance transition  
373 was also recognized in the eccentricity band power curve and the total power curve (Fig. 7f, g).  
374 These observed eccentricity AM shifts are coincident in timing with La2004 astronomical  
375 solution during this period (Laskar et al., 2004), and might show some potential linkages  
376 between the unique celestial configuration and the geological events, such as OAE3 (Ma et al.,  
377 2017; Wu et al., 2022). In contrast, the eccentricity band power curve in the SK-1n core (76-65  
378 Ma) appears noisier, with no obvious ~2.4 Myr eccentricity AM cycles observed (Fig. 7f), the  
379 reasons might be ascribed to the different astronomical response at different stages of Basin's  
380 evolution and the uncertainties in the temporal calibration. However, two high eccentricity power  
381 intervals have been identified in the Mingshui Formation (Fig. 7f), which roughly corresponding  
382 to the paleo-lake transgressive stage (Gao et al., 2015). In addition, a significant global cooling  
383 event at approximately 70 Ma, reflected by a pronounced positive oxygen isotope excursion in  
384 benthic foraminifera (Miller et al., 2005; Friedrich et al., 2012), was also recognized by the  
385 pedogenic carbonate oxygen isotope in the Songliao Basin (Gao et al., 2015, 2021). A typical  
386 lake shrink interval was also inferred from the DYNOT result, which roughly corresponding to  
387 the low eccentricity power and high obliquity power interval (Fig. 7h). Afterward, this cooling  
388 interval was terminated by a transient climatic warming in the middle Maastrichtian (ca.  
389 69.5-68.5 Ma), which marked by the increased marine bottom water temperature (Jung et al.,  
390 2013; Mateo et al., 2017). Interestingly, this warming period was timely associated with the high  
391 eccentricity power interval (Fig. 7), indicating the high sensitivity of eccentricity to the warm

392 climatic and depositional processes (Wu et al., 2022).

393 The obliquity band power in the SK-1 core (91.97-65.06 Ma) and obliquity/total power both  
394 reveal ~1.2 Myr cycle, although it is not persistent throughout the entire study interval (Fig. 7c,  
395 d). The lower part of the Qingshankou Formation (ca. 91.9-88.5 Ma) displays a high obliquity  
396 signal and a distinct ~1.2 Myr obliquity AM cycle (Fig. 7c, d). Huang et al. (2021a) have  
397 proposed a threshold clipping amplified model to interpret the low-amplitude AM signals in  
398 geological records, which also hints that the strong obliquity signal is favorable for preserving  
399 low frequency AM cycles (e.g., Levy et al., 2019; Huang et al., 2020, 2021a). Additionally, the  
400 integrate obliquity band power suggests the absence of a strong 1.2 Myr obliquity cycle at  
401 around 84 Ma which timely associated with the resonance transition (Fig. 7d). This phenomenon  
402 was firstly documented in the Libsack FMI record in North America, which means the resonance  
403 state may suggest a transient change in the sensitivity of the climate or sedimentary system to  
404 obliquity forcing at a global scale (Ma et al., 2017). In the Songliao Basin, this transition  
405 corresponds to a rapid shift from shallow (Yaojia Fm.) to deep lake (Nenjiang Fm.) condition and  
406 associated with increased organic carbon burial and marine incursion events (Fig. 7).

407 To our knowledge, no previous studies employed integrated precession band power derived  
408 from astronomical tuned time series to examine paleoclimatic changes. The main reason for this  
409 might be ascribed to the fact that the amplitude of the precession has been modulated by  
410 eccentricity, and thus it is difficult to separate the variation of the precession caused by the  
411 different depositional settings from the eccentricity itself. Besides, in high frequency bands, the  
412 sedimentary noise tends to superimpose on astronomical signals (Hajek and Straub, 2017). Here,  
413 we have attempted to retrieve the precession band power from the Th time series (Fig. 7b).  
414 According to the integrate precession band power curve, we have not observed any discernible

415 periodical orbital signals (Fig. 7b), but the precession band signal exhibited relatively high power  
416 during the deposition of the Yaojia and Mingshui Formations compared to other periods (Fig. 7b).  
417 However, during the high precession band power intervals, the corresponding eccentricity band  
418 power is relatively low (Fig. 7f), which does not conform with the eccentricity-precession  
419 modulation effect. This may suggest these high precession band power intervals were not only  
420 included the orbital precession signals, but also existed regular sedimentary relative small-scale  
421 autocyclicities (Hajek and Straub, 2017). As we noticed, these high precession band power  
422 intervals are corresponded to the shallow lake and meandering river facies, these sedimentary  
423 environments indicate a shallow water condition, which is also confirmed by the DYNOT result  
424 (Fig. 7h). Therefore, we posit that the high precession band power intervals are partly influenced  
425 by the autogenic sedimentation processes, and this will be discussed in the following section.

### 426 **5.3 Different orbital power ratio distributions in varied sedimentary environments**

427 Within the context of sedimentary facies division, we have calculated the average orbital  
428 power ratio distributions for different facies intervals by applying the RAOPR method (Fig. 8,  
429 S4; Table. 1). For the deep lake facies, we have found that the eccentricity and precession power  
430 ratios were different between Qingshankou and Nenjiang formations. To interpret these  
431 discrepancies, we consider the local geological events have played a major role in recording and  
432 preserving the orbital signals. According to the depositional background, the lower part of  
433 Nenjiang Formation has been disturbed by the intermittent marine incursion events (Hu et al.,  
434 2015), which could change the equilibrium of the lake biogeochemistry (Wang et al., 2015).  
435 Recently, Huang et al (2021a) have proposed a biogeochemical threshold clipping response  
436 model to explain the ~40 kyr obliquity transformed to ~173 kyr obliquity AM cycle, and

437 considered the disturbance of lake biogeochemical conditions can change the orbital signal  
438 components. In addition, model simulation results confirmed that the non-linear accumulation or  
439 bioturbation effects also can transform the precession-forced carbonate cycle into eccentricity  
440 band (Ripepe and Fischer, 1991). Therefore, the low precession and high eccentricity bands  
441 signal in the first and second member of Nenjiang Formation may indicate the marine incursion  
442 events have altered the original orbital signal components. Besides, we also noticed that, the two  
443 deep lake facies intervals have the highest obliquity power ratio in this ~24 Myr-long  
444 sedimentary record. Considering the paleogeographic location of the Songliao Basin, the  
445 obliquity may play a major role in modulating the hydrological cycle through controlling  
446 meridional insolation circulation and enhancing poleward moisture transport (Raymo and  
447 Nisancioglu, 2003). The ~173 kyr obliquity AM cycle has been both detected in the  
448 Qingshankou TOC series (Huang et al., 2021a) and Nenjiang chemical weathering proxies (Li et  
449 al., 2022), which further confirmed that the obliquity forced the Songliao paleo-lake hydrological  
450 variations and controlling the organic carbon burial (Huang et al., 2021a).

451 From the Qingshankou to Yaojia formations, the Songliao paleo-lake water depth was  
452 decreased, which is demonstrated both by the sedimentary facies analysis and DYNOT  
453 lake-level modelling (Fig. 7h). Theoretically, the shallow lake environment should have relative  
454 lower orbital signals than the deep lake depositional environment, because the sedimentary noise  
455 was higher in shallow water than deep water (Li et al., 2018; Wang et al., 2020). So, it would be  
456 abnormal for shallow lake facies owning high precession power ratio, as well as its modulation  
457 signal in eccentricity band. This abnormal feature indicates that the high precession power in the  
458 Yaojia formation was not only originated from the Earth's orbital precession forcing. In contrast,  
459 there are some specific sedimentary processes to generate the precession-like signals. Previous

460 studies demonstrated that autogenic processes could destroy orbital-scale signals in some  
461 specific sedimentary environments and some periodicities produced by autogenic variability  
462 might be confused with orbital forcing (Jerolmack and Paola, 2010; Li et al., 2016; Hajek and  
463 Straub, 2017). Especially, the simulation experiment of lake formation and infilling in the  
464 maximum subsidence zone indicated about  $10^4$ - $10^5$  years autogenic variability (Kim and Paola,  
465 2007). Therefore, the autogenic process might reasonably explain the high precession power  
466 ratio in the Yaojia Formation.

467 As the Songliao paleo-lake shranked, the upper part of the Nenjiang Formation and the  
468 whole Sifangtai and Mingshui formations were deposited from delta to meandering river  
469 environments (Wang et al., 2013). The average eccentricity power ratio was increased and  
470 precession power ratio was reduced from the Nenjiang Formation to Mingshui Formation (Fig.  
471 8). From the MTM spectrum results, we also found that the precession band signals do not reach  
472 to the autoregressive lag-1 stochastic noise model testing (Fig. 4). This orbital signal component  
473 is prevalent in the progradational and retrogradational trends of the alluvial-delta-lacustrine  
474 systems. For example, the Late Eocene to Middle Miocene delta sequence in the Ebro Basin  
475 (Valero et al., 2014) and the Middle Miocene Madrid Basin (Abels et al., 2009) both show a  
476 significant power at eccentricity bands but no obvious precession signals existed. Moreover, in  
477 the coal-bearing terrestrial successions, the occurrence of coal intervals is often linked to the  
478 eccentricity driven forcing, while the precession index can barely be identified (e.g., review by  
479 Oplustil et al., 2022). All of these features indicated the high frequency orbital signals can hardly  
480 preserve in continental shallow water environments. Suppose that there is a regularly  
481 sedimentary process (e.g., the balance between sediment supply and subsidence) to erase the  
482 high-frequency orbital signals before they preserved in the stratigraphic succession, this

483 “depositional clipping function” would impose a rectification effect on the original signal  
484 (Ripepe and Fischer, 1991; Hinnov, 2018; Huang et al., 2021a). In addition, the non-linear  
485 sedimentary response (e.g., bioturbation and/or lake geochemistry equilibrium) will further  
486 amplify the low frequency signals and eradicate the high frequency index (Ripepe and Fischer,  
487 1991; Hinnov, 2018; Huang et al., 2021a). Therefore, in the terrestrial delta and/or meandering  
488 river facies, the low frequency orbital signals (e.g., ~400 kyr and 100 kyr eccentricity) could be  
489 preserved but the high frequency signals (e.g., ~20 kyr precession) might often be erased.

490 In general, from the orbital signal components of different sedimentary facies intervals, we  
491 considered that the Yaojia, Nenjiang (3-5 members), Sifangtai and Mingshui formations might be  
492 disturbed by autogenic processes, such as river migration, delta growth, lake transgressive and  
493 regressive phases. The Nenjiang (3-5), Sifangtai and Mingshui formations displayed high power  
494 in eccentricity bands and low power in precession bands, suggesting that meandering river  
495 environments may not record precession signals or that post-depositional processes have erased  
496 them. While the Yaojia Formation has shown the highest precession band power among the five  
497 stratigraphic intervals (Fig. 8c), which means the local depositional processes has generated  
498 regular periodic signals at about ten-thousands time scale. The lower part of the Nenjiang  
499 Formation has disturbed by the marine incursion events, which greatly changed the orbital signal  
500 components through the intrabasinal processes. The Qingshankou Formation represented the  
501 most stable lake depositional environment, its orbital signal component might reflect the original  
502 climatic information, although some orbital amplitude modulation cycle associated with  
503 allogenic processes have been found in other paleoclimatic proxies (e.g., Huang et al., 2021a).

#### 504 **5.4 Astronomical climate-deposition transfer processes in terrestrial depositional systems.**

505 Resolving astronomical signals from stratigraphic records is always challenging, because  
506 there are many complex factors that influence the orbital signal propagating into geological  
507 archives (Strasser et al., 2006; Meyers et al., 2008; Hinnov, 2013). Thus, a thorough  
508 astrochronological evaluation necessitates careful consideration of astronomical, geological,  
509 climatic, and statistical aspects (Meyers, 2019; Sinnesael et al., 2019; Wouters et al., 2022; Wang  
510 Y et al., 2023).

511 In light of the aforementioned considerations, we have reconsidered some fundamental  
512 issues in the realm of cyclostratigraphy, especially the interpretation of the environmental  
513 periodic signals from continental sedimentary settings. Generally, a complete terrestrial  
514 sedimentary system mainly includes three elements: sediment supply, sediments transport and  
515 accommodation space (Fig. 9) (Carroll and Bohacs, 1999; Allen, 2008). The topographic gradient  
516 resulting from tectonic dynamics represents the first-order control on the spatial distribution of  
517 uplift and subsidence on the Earth's surface, while the rate and mass of material transport is  
518 contingent upon climate (Hajek and Straub, 2017). Therefore, the tectonic processes in the  
519 source area and climatic variations can affect the sediment and water supply. In the vicinity of  
520 the source region, we usually cannot detect any periodic environmental signals (Fig. 9).  
521 Terrestrial sediment transport networks mainly comprise the fluvial and aeolian systems, and for  
522 sedimentary archives deposited under aeolian conditions, environmental signals are typically  
523 associated with the orbital-monsoon system (e.g., An et al., 1991). As for fluvial systems, that  
524 usually move and reconfigure themselves at the orbital temporal scales (Kim et al., 2010).

525 In natural systems, an important endeavor is to decipher which types and scales of rhythmic

526 stratal patterns are reflective of internal dynamics of terrestrial environments, and how to  
527 effectively differentiate between internal periodic variations and orbital signals. Fortunately, the  
528 natural autogenic cyclicities would not produce strong enough power signals in the spectrum  
529 periodogram (Hajek and Straub, 2017; Huang et al., 2020), and the improved understanding of  
530 the autogenic dynamics (e.g., Wang Y et al., 2023) could help constrain the potential autogenic  
531 signals and build improved or new statistical tests to detecting astronomical climate cycles. To  
532 this end, we present a flexible guideline for identifying orbital signals from terrestrial strata that  
533 have formed in varying sedimentary contexts. In practice, the power spectrum of proxies should  
534 be examined, and null-hypothesis statistical models and confidence tests that are better-suited  
535 should be constructed (e.g., ASM, MTM, FFT, COCO and eCOCO). Additionally, the amplitude  
536 modulation effect between eccentricity and precession provides a robust solution for  
537 discriminating orbital signals from autogenic cyclicity (TimeOpt and eTimeOpt, testPrecession).  
538 Moreover, combining the integrate power and RAOPR methods enables the tracking of orbital  
539 power variations and identification of the orbital signal distributions from strata. And finally, by  
540 utilizing the distinctive features of abnormal signal alteration and taking into account the relevant  
541 sedimentary conditions, we can proficiently discern whether the periodical signal in the  
542 geological record has been subject to modification through sedimentation processes.

## 543 **6. CONCLUSION**

544 In this study, we present a new method called the Random-length Average Orbital Power  
545 Ratio calculation (RAOPR). This method expands the more established power integration  
546 method that investigates changes in astronomical frequencies by integrating their respective

547 frequency ranges over a stratigraphic signal by repeating the calculation over many different  
548 window lengths, and thus reducing the sensitivity to the theoretical inherent long-term signals.  
549 Through an investigation of the distributions of orbital power ratios across various levels of  
550 synthetic Eccentricity-Tilt-Precession (ETP) series with the inclusion of noise, we have been  
551 able to unambiguously identify distinct distributions of orbital power ratios within these merged  
552 ETP+noise series. As such, it could be a powerful tool for identifying the orbital signals that  
553 have been modified by depositional environment changes.

554 By analyzing astronomically-tuned Th logging data from the terrestrial Songliao Basin, we  
555 uncovered distinctive orbital power ratio distributions that are associated with different  
556 depositional environments. By integrating these findings with geological information, we were  
557 able to infer the types of depositional processes that impacted the recording and preservation of  
558 the orbital signals. For example, we found that the marine incursion events in the lower part of  
559 the Nenjiang Formation led to a decrease in precession signal power. The unexpectedly high  
560 precession band power observed in the Yaojia Formation may imply that autogenic processes  
561 played a substantial role in generating precession-like autocyclicity. Furthermore, the high power  
562 in eccentricity bands and very low power in precession bands observed in the Sifangtai and  
563 Mingshui formations suggested that high-frequency orbital signals can be challenging to  
564 preserve in shallow water environments. Taken together, these findings underscore the complex  
565 interactions between orbital forcing and climatic/depositional feedbacks, and highlight the  
566 importance of geological factors such as depositional environments, sediment transport processes,  
567 and local geological events when assessing orbital signals from stratigraphic successions.

568

569

570

571 Table. 1. The average orbital power ratios and their standard deviation values calculated from the  
572 SK-1 tuned Th time series.

Formations	Sediment ary facies	eccentricity power ratio	Standard ( $2\delta$ )	obliquity power ratio	Standard ( $2\delta$ )	precession power ratio	Standard ( $2\delta$ )
Qingshankou	DL	0.289	0.004	0.345	0.0052	0.152	0.0042
Yaojia	SL	0.315	0.0094	0.151	0.0032	0.226	0.0072
Nenjiang(1+2)	DL	0.41	0.0092	0.331	0.0102	0.053	0.0024
Nenjiang(3-5)	DEL-MR	0.401	0.0042	0.187	0.006	0.143	0.0018
Sifangtai	MR	0.427	0.0092	0.271	0.0078	0.095	0.0018
Mingshui	MR	0.591	0.0074	0.173	0.006	0.046	0.002

573

574

575

576

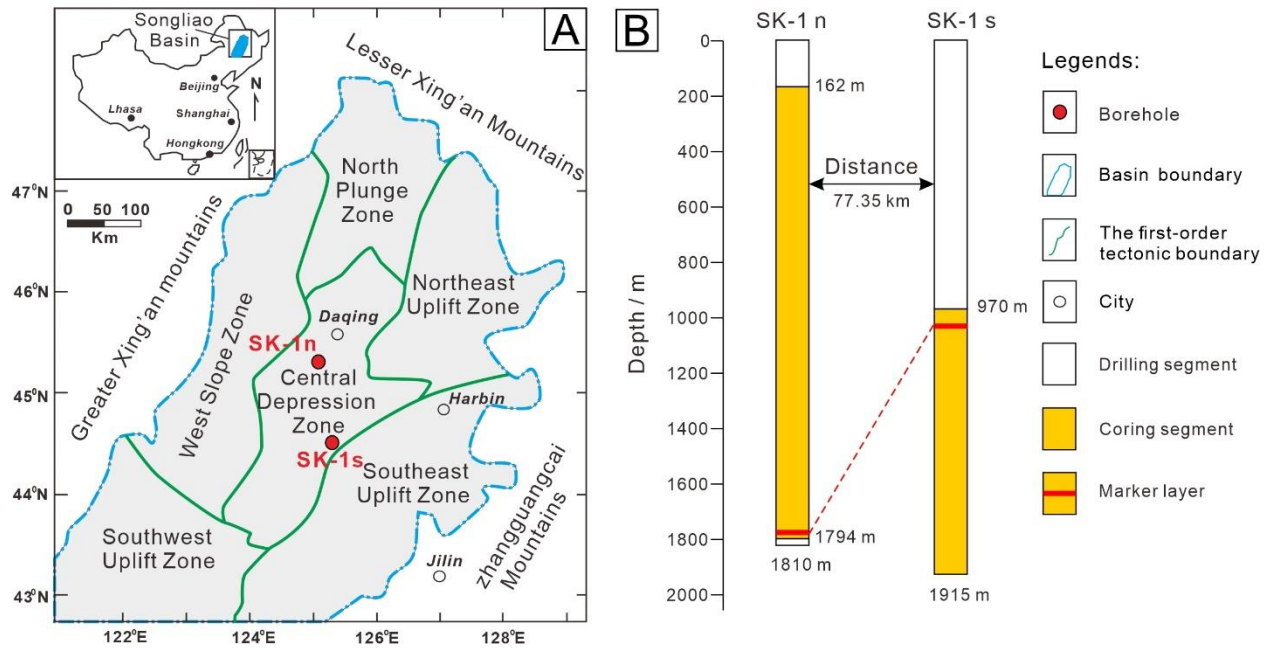
577

578

579

580 **FIGURE CAPTURES**

581



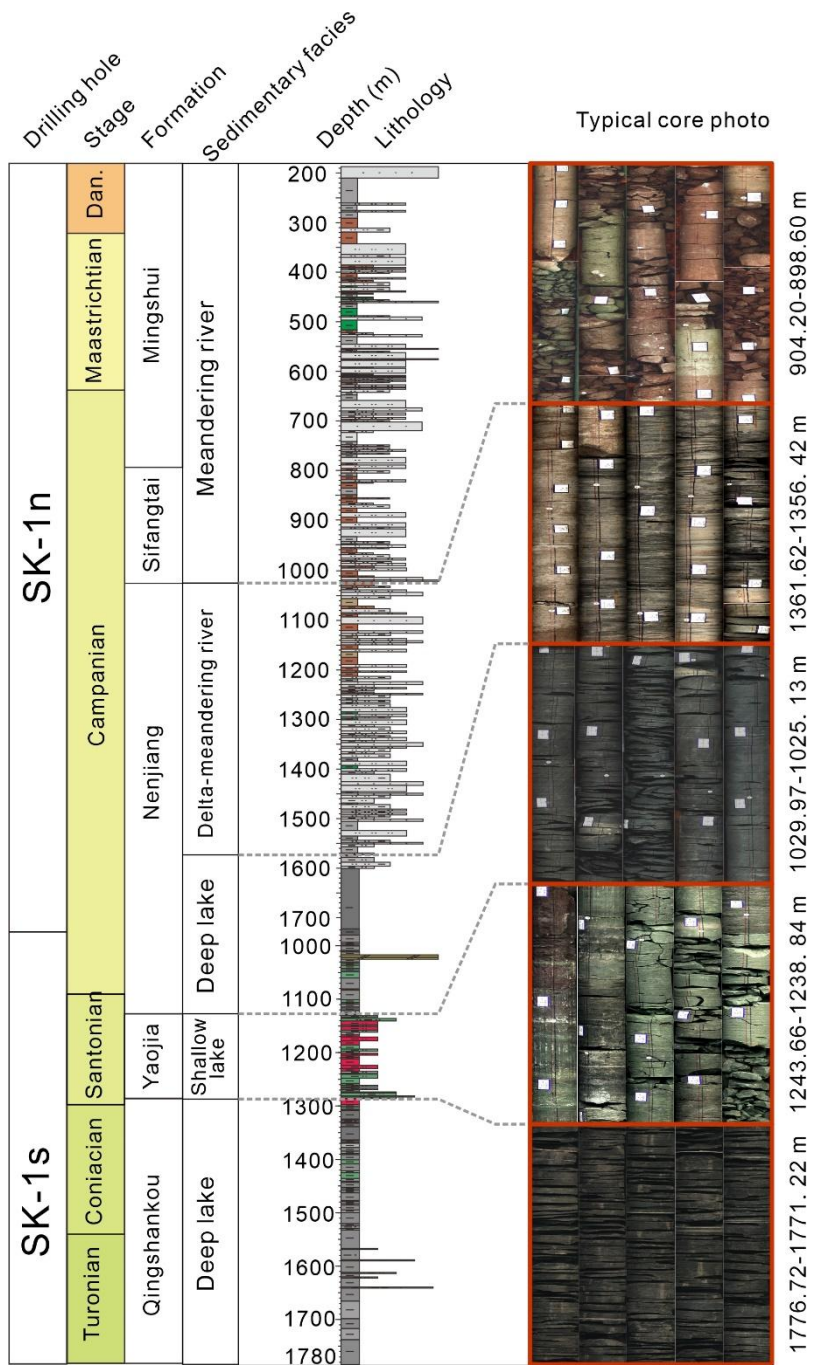
582

583 **Fig. 1.** The geological setting of the Songliao Basin and SK-1 core. (A) The Songliao Basin of

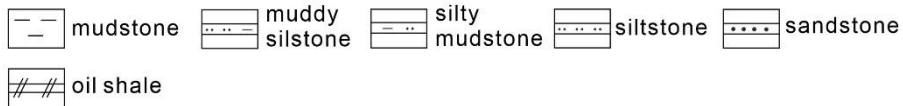
584 Northeast China, including its geographic extent, and first-order geomorphic elements (modified

585 from Feng et al., 2010). (B). The core correlation of SK-1s and SK-1n borehole (modified from

586 Feng et al., 2010).



Legends:



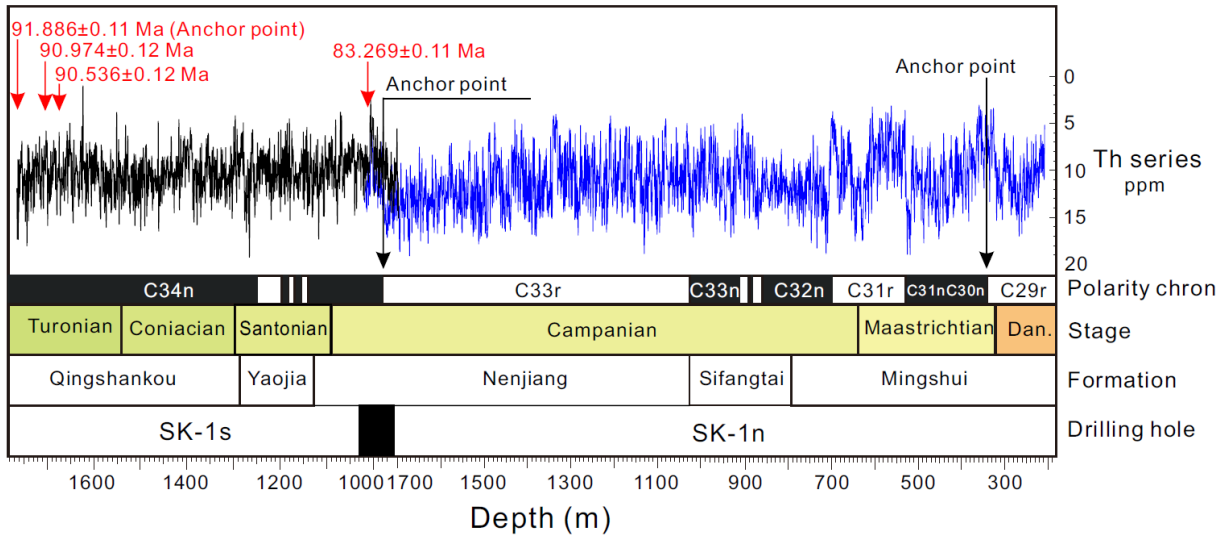
587

588 **Fig. 2.** The strata information, sedimentary facies and typical core photos of the SK-1 composite

589 drilling core. The lithological association and sedimentary facies were modified from Wang C et

590 al. (2013). The x-axis on the lithology section represents the different grain size and the color in

591 these lithologies indicate different lithological color features.



592

593 **Fig. 3.** The chronostratigraphic framework and astronomical tuning anchored points of SK-1

594 core. The polarity chronology was cited from Deng et al. (2013); the red arrows were

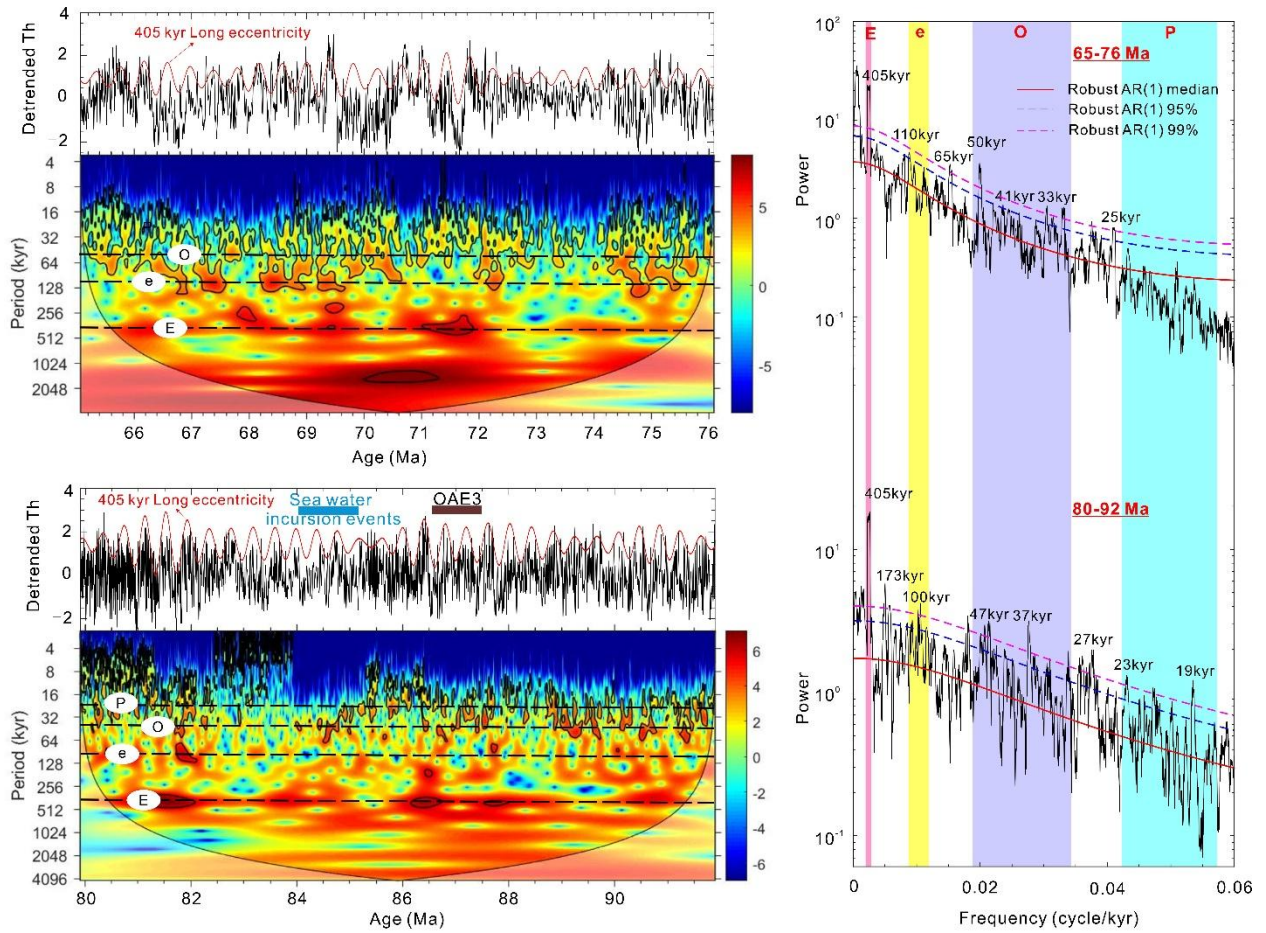
595 CA-ID-TIMS U-Pb ages (Wang T et al., 2016), especially the age around 1780 m ( $91.886\pm 0.11$

596 Ma) was used as anchored point for astronomical tuning for SK-1s core (Wu et al., 2022), while

597 the C34n/C33r and C30n/C29r boundary (Deng et al., 2013) were used as anchored points for

598 orbital tuning in the SK-1n core (Wu et al., 2014). The black line represents the SK-1s core

599 logging Th series while the blue line is the SK-1n core logging Th series.



600

601 **Fig. 4.** The multi-taper method (MTM; Thomson, 1982) with a red noise null model (Mann and

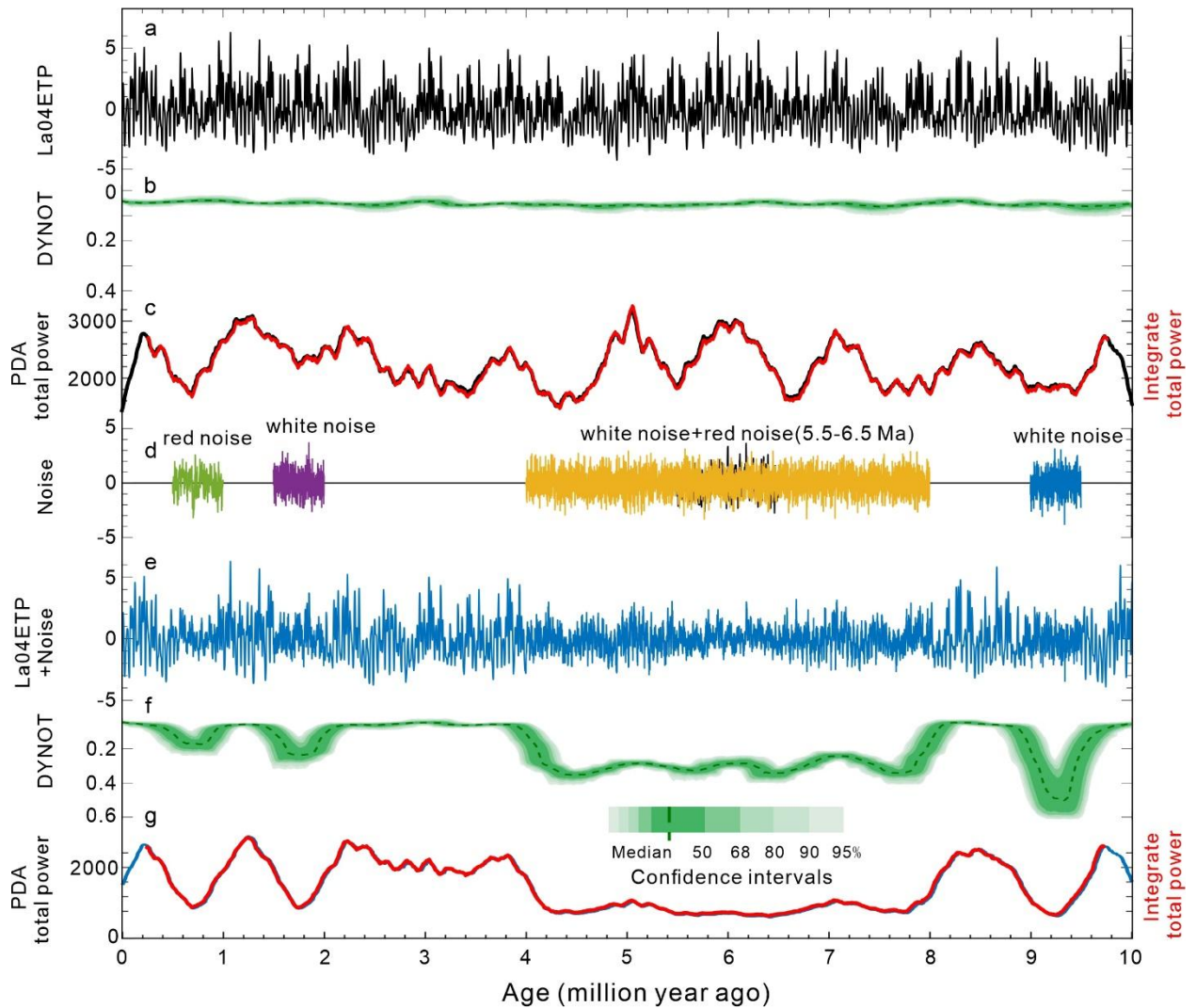
602 Lees, 1996) and the wavelet spectral analysis (Torrence and Compo, 1998) were applied for

603 seeking the orbital signals in Th time series (data from Wu et al., 2014, 2022). The long

604 eccentricity signals were extracted from the stratigraphic series using a Gaussian bandpass filter

605 with a bandwidth at  $0.002\text{-}0.003 \text{ kyr}^{-1}$ . Note: for the MTM analysis, the discrete prolate

606 spheroidal sequences (DPSS) is set to  $(2*tbw)-1$ , where  $tbw=2$ ,  $tbw$ : time-bandwidth.



607

608 **Fig. 5.** Evaluation of the total orbital power variations from the synthetic stratigraphic noise

609 model. (a) ETP from 0-10 Ma (Laskar et al., 2004). (b) DYNOT model of ETP. (c) calculation of

610 the orbital power variations by using the power decomposition analysis (black line) and

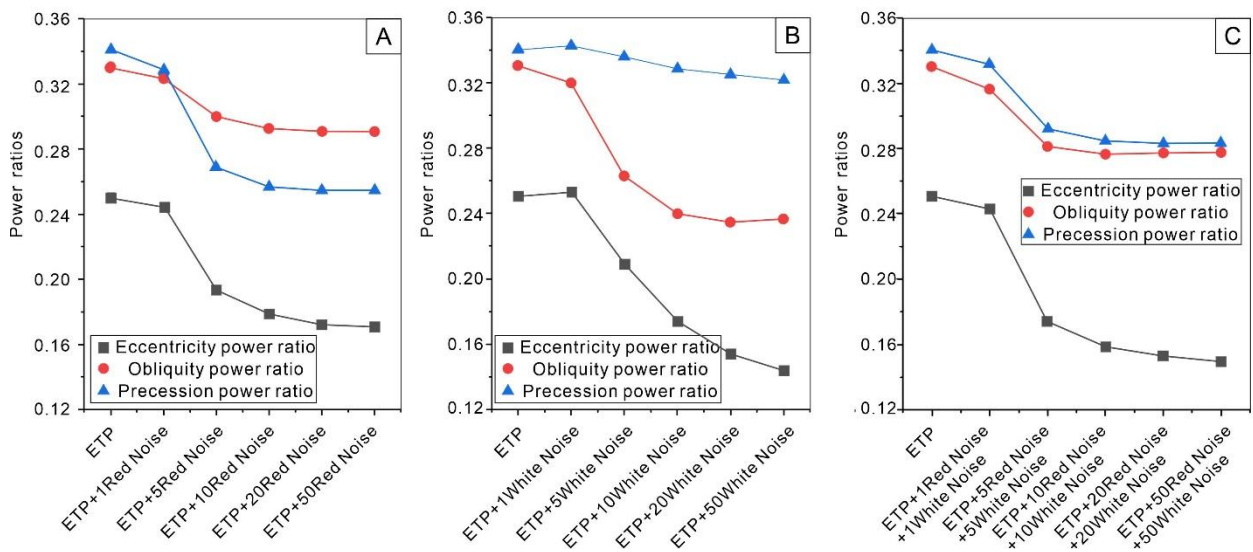
611 *integratePower* algorithm (red line). (d) Four interval with different types of noise. (e) Merged

612 the ETP and noise. (f) DYNOT model of the merged series, confidence levels are estimated by a

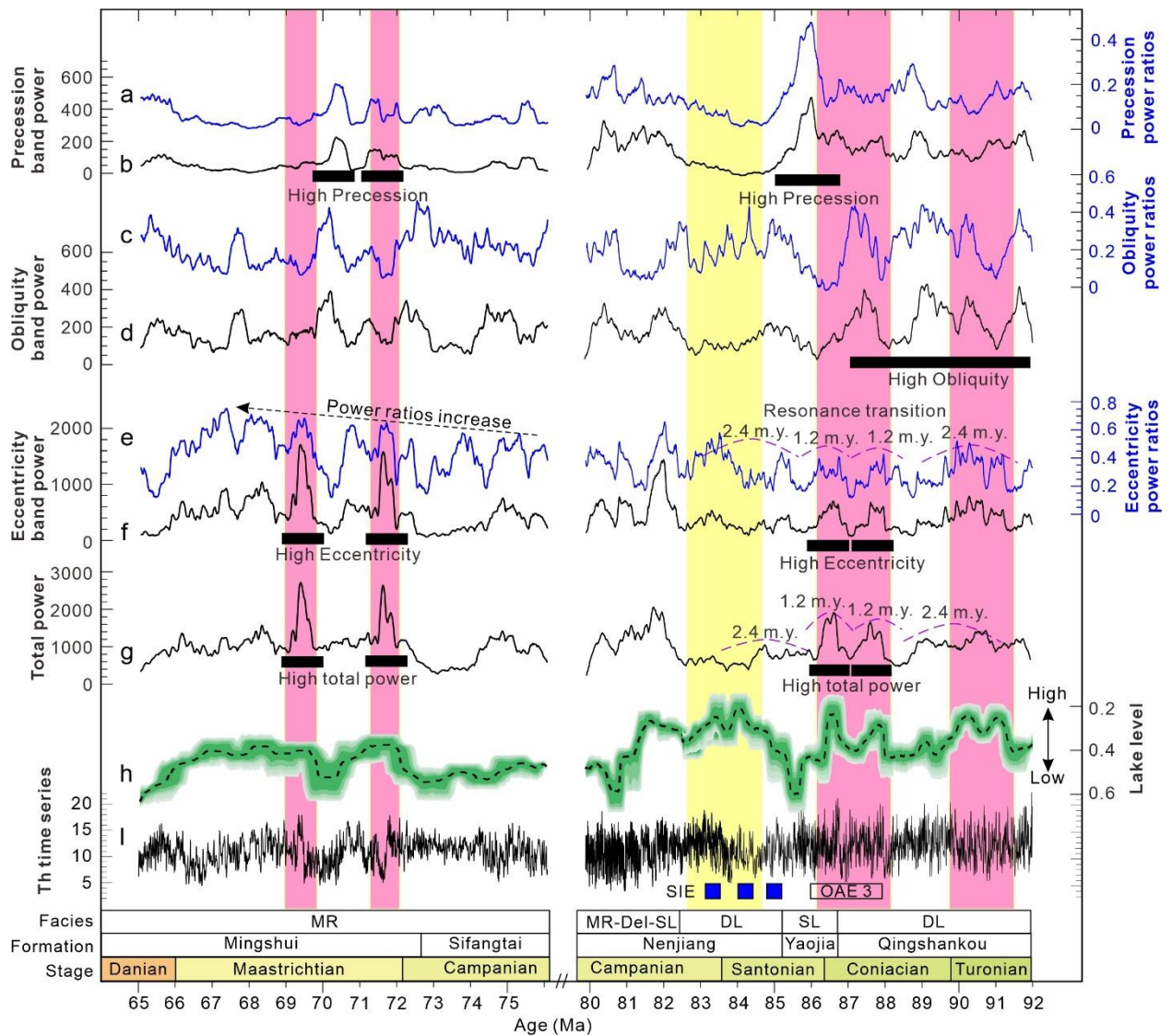
613 Monte Carlo analysis with 2,000 iterations and a running window of 400 kyr. (g) Evaluation the

614 orbital power variation from the merged time series.

The orbital power ratios in ETP plus noise series



615  
 616 **Fig. 6.** The average orbital power ratios in different ETP plus noise modeling time series. (A)  
 617 Evaluation of the eccentricity, obliquity and precession average power ratios from the synthetic  
 618 ETP+red noise series; (B) Calculation of the eccentricity, obliquity and precession average  
 619 power ratios from the synthetic ETP+white noise series; (C) Calculate the eccentricity, obliquity  
 620 and precession average power ratios from the synthetic ETP+red+white noise series



621

622 **Fig. 7.** The long-term evolution of the orbital signal power and power ratio retrieved from the

623 SK-1 borehole astronomically-tuned Th time series (Wu et al., 2014; 2022). The eccentricity,

624 obliquity and precession band power (b, d, f), power ratios (a, c, e) and total orbital power (g)

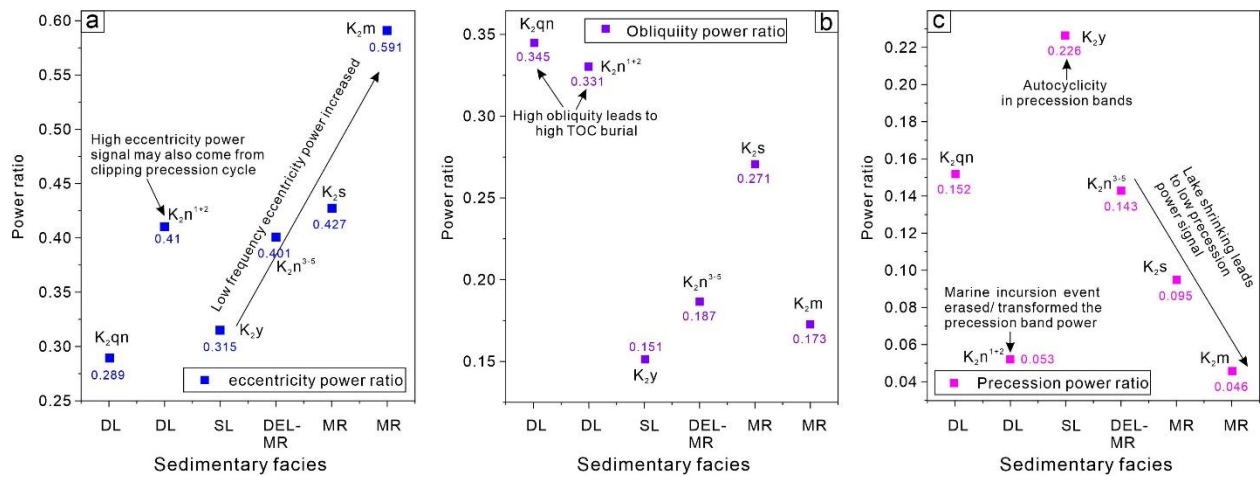
625 were calculated by the PDA method in *Acycle* free software (Li et al., 2019a). The simulated

626 lake-level was obtained by using the DYNOT methods (h). The purple areas indicate high lake

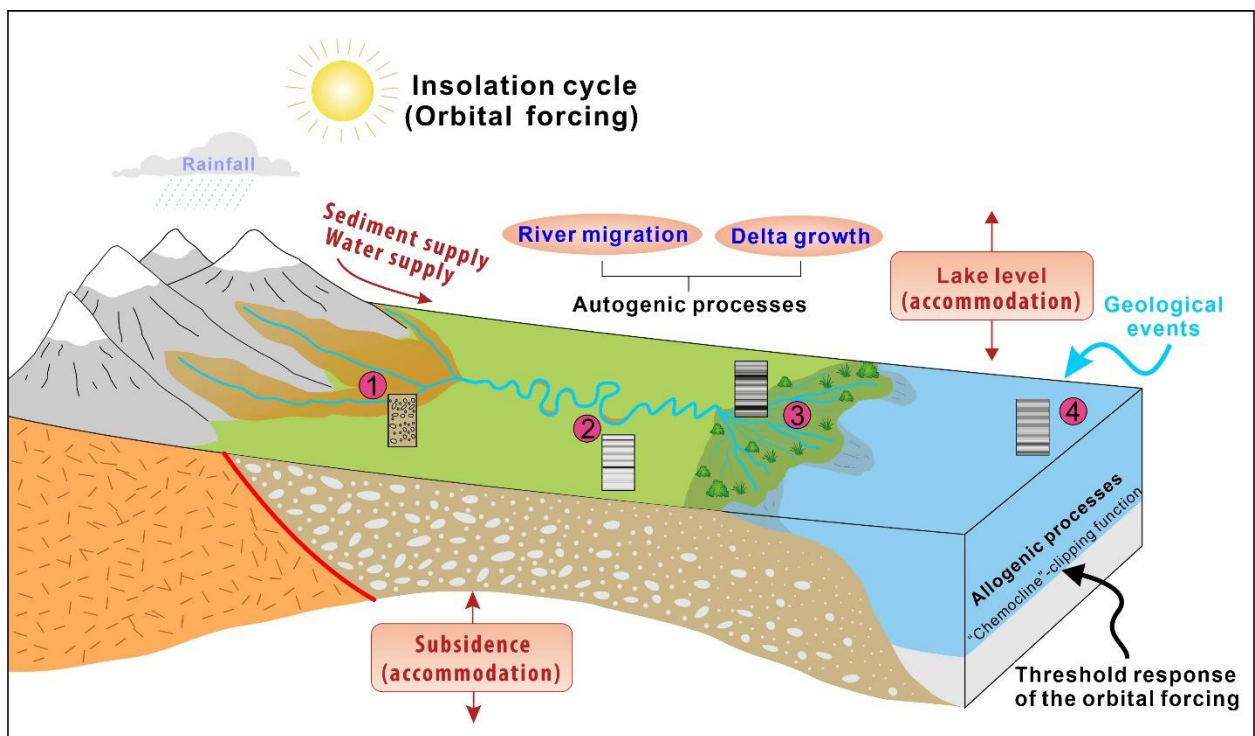
627 level associated with high orbital power, while the yellow area represents the high lake level

628 corresponding to the low orbital signal power interval. DL: deep lake facies; MR: meandering

629 river facies; SL: shallow lake facies; Del: delta facies.



630  
 631 **Fig. 8.** The average orbital power ratios in different formations (or different sedimentary facies  
 632 intervals). (a). the average eccentricity power ratios; (b). the average obliquity power ratios; (c).  
 633 the average precession power ratios.



634  
 635 **Fig. 9.** The conceptual pictures showing the interaction of orbital forcing and terrestrial  
 636 depositional processes (modified from Hajek and Straub, 2017). A complete terrestrial  
 637 depositional system associated with external and internal factors to control the  
 638 sediment-transport-deposit processes. The 1-4 lithologies are roughly represent the typical  
 639 lithological association which varied from different depositional environments (i.e., 1-alluvial

640 fan, 2-meandering river, 3-delta, 4-lacustrine).

641

## 642 **ACKNOWLEDGMENTS**

643 We thank Brad Singer and M. Smith for carefully handled our manuscript. We also thank two  
644 anonymous reviewers for helpful and constructive comments, which have greatly improved our  
645 work. This study was financially supported by the National Natural Science Foundation of China  
646 (Grant Nos. 41888101, 42302122, 42172137, 41972096, 42050102 and 42050104), Sichuan  
647 Provincial Youth Science & Technology Innovative Research Group Fund (No. 2022JDTD0004),  
648 Deep-time Digital Earth (DDE) Big Science Program and Everest Scientific Research Program  
649 of Chengdu University of Technology (Grant No. 10912-KYQD202209480). He Huang Thanks  
650 Chengdu University of Technology (CDUT) provides the financial support (Grant No.  
651 21700-000504) for visiting the IMCCE, CNRS, Observatoire de Paris, France. Matthias  
652 Sinnesael thanks European Research Council (ERC) under the European Union's Horizon 2020  
653 Research and Innovation Program (Advanced Grant AstroGeo-885250) for funding.

654

## 655 **REFERENCES CITED**

656 Abels, H.A., Aziz, H.A., Krijgsman, W., Smeets, S.J.B., Hilgen, F.J., 2010, Long-period  
657 eccentricity control on sedimentary sequences in the continental Madrid Basin (middle  
658 Miocene, Spain): Earth and Planetary Science Letters, v. 289, p. 220-231.  
659 Abels, H. A., Kraus, M. J., Gingerich, P. D., and Sheldon, N., 2013, Precession-scale cyclicity in

660 the fluvial lower Eocene Willwood Formation of the Bighorn Basin, Wyoming (USA):  
661 Sedimentology, v. 60, p. 1467-1483.

662 Allen P.A., 2008, From landscapes into geological history: Nature, v. 451(7176), p. 274-276,  
663 <https://doi.org/10.1038/nature06586>

664 An, Z., Kukla, G., Porter, S., & Xiao, J., 1991, Magnetic susceptibility evidence of monsoon  
665 variation on the Loess Plateau of central China during the last 130,000 years: Quaternary  
666 Research, v. 36(1), p. 29-36. doi:10.1016/0033-5894(91)90015-W.

667 Bazykin DA, Demicco RV, Hardie LA., 1997, Autocycles vs. allocycles in shallow marine  
668 carbonate platform deposits: insights from 2-dimensional computer modelling  
669 experiments: Gaea Heidelbergensis 3:66

670 Carroll, A. R. and Bohacs K. M., 1999, Stratigraphic classification of ancient lakes: Balancing  
671 tectonic and climatic controls: Geology, v. 27: p. 99-102.

672 Deng, C.L., He, H.Y., Pan, Y.X., Zhu, R.X., 2013, Chronology of the terrestrial Upper Cretaceous  
673 in the Songliao Basin, Northeast Asia: Paleogeogr. Paleoclimatol. Paleoecol., v. 385, p.  
674 44–54. <https://doi.org/10.1016/j.palaeo.2012.07.028>.

675 Feng, Z., Jia, C.Z., Xie, X.N., Zhang, S., Feng, Z.H., Cross, T.A., 2010, Tectonostratigraphic units  
676 and stratigraphic sequences of the nonmarine Songliao basin, northeast China: Basin Res.,  
677 v. 22, p. 79–95, <https://doi.org/10.1111/j.1365-2117.2009.00445.x>.

678 Friedrich, O., Norris, R.D., Erbacher, J., 2012, Evolution of middle to late Cretaceous oceans—a  
679 55 m.y. record of Earth’s temperature and carbon cycle: Geology, v. 40, p. 107–110,  
680 <https://doi.org/10.1130/G32701.1>.

681 Gao, Y., Ibarra, D.E., Wang, C., Caves, J.K., Chamberlain, C.P., Graham, S.A., Wu, H., 2015,  
682 Mid-latitude terrestrial climate of East Asia linked to global climate in the late Cretaceous:

683 Geology, v. 43, p. 287–290, <https://doi.org/10.1130/G37574Y.1>.

684 Gao, Y., Ibarra, D.E., Caves Rugenstein, J.K., Chen, J., Kukla, T., Methner, K., Gao, Y., Huang,  
685 H., Lin, Z., Zhang, L., Xi, D., Wu, H., Carroll, A.R., Graham, S.A., Chamberlain, C.P.,  
686 Wang, C., 2021, Terrestrial climate in mid-latitude East Asia from the latest Cretaceous to  
687 the earliest Paleogene: A multiproxy record from the Songliao Basin in northeastern  
688 China: *Earth-Science Reviews*, v. 216, 103572.

689 Hasselmann, K., 1976, Stochastic climate models: Part I. Theory: *Tellus*, v. 6, p. 473–485.

690 Hays, J.D., Imbrie, J., Shackleton, N.J., 1976, Variations in the Earth's orbit: pacemaker of the ice  
691 ages: *Science*, v. 194, p. 1121–1132, <https://doi.org/10.1126/science.194.4270.1121>.

692 Hajek, E.A., Straub, K.M., 2017, Autogenic sedimentation in clastic stratigraphy: *Annu. Rev.*  
693 *Earth Planet. Sci.*, v. 45, p. 681–709.

694 Hinnov, L.A., 2000, New perspectives on orbitally forced stratigraphy: *Annu. Rev. Earth Planet.*  
695 *Sci.*, v. 28, p. 419-475.

696 Hinnov, L. A and Hilgen, F. J., 2012, Cyclostratigraphy and Astrochronology: *The Geologic Time*  
697 *Scale*, Chapter 4.

698 Hinnov, L.A., 2013, Cyclostratigraphy and its revolutionizing applications in the earth and  
699 planetary sciences: *Geological Society of America Bulletin*, v. 125, p. 1703-1734.

700 Hinnov, L., 2018, Cyclostratigraphy and Astrochronology in 2018: *Stratigraphy & Timescales*,  
701 Volume 3, ISSN 2468-5178.

702 Hu, J.F., Peng, P.A., Liu, M.Y., Xi, D.P., Song, J.Z., Wan, X.Q., Wang, C.S., 2015, Seawater  
703 Incursion Events in a Cretaceous Paleo-lake Revealed by Specific Marine Biological  
704 Markers: *Sci Rep.*, v. 5, p. 9508.

705 Huang, H., Gao, Y., Jones, M.M., Tao, H., Carroll, A.R., Ibarra, D.E., Wu, H., Wang, C., 2020,

706           Astronomical forcing of Middle Permian terrestrial climate recorded in a large paleolake in  
707           northwestern China: *Palaeogeography, Palaeoclimatology, Palaeoecology*, v. 550, 109735.

708   Huang, H, Gao, Y, Ma, C, Matthew M. Jones, Christian Zeeden, Daniel E. Ibarra, Wu Huaichun,  
709           Wang Chengshan, 2021a, Organic carbon burial is paced by a ~173-ka obliquity cycle in  
710           the middle to high latitudes: *Science Advances*, v. 7, eabf9489.

711   Huang, H, Gao, Y, Ma, C, Niu, L, Dong, T, Tian, X, Cheng, H, Hei, C. L, Tao, H. F, Wang, C. S,  
712           2021b, Astronomical constraints on the development of alkaline lake during the  
713           Carboniferous-Permian Period in North Pangea: *Global and Planetary Change*, v.207, p.  
714           103681.

715   Jerolmack, D. J. and Paola, C., 2010, Shredding of environmental signals by sediment transport:  
716           *Geophys. Res. Lett.*, v. 37, L19401.

717   Jung, C., Voigt, S., Friedrich, O., Koch, M.C., Frank, M., 2013, Campanian-Maastrichtian Ocean  
718           circulation in the tropical Pacific: *Paleoceanography*, v. 28, p. 562–573.  
719           <https://doi.org/10.1002/palo.20051>.

720   Kim, W. and Paola, C., 2007, Long-period cyclic sedimentation with constant tectonic forcing in  
721           an experimental relay ramp: *Geology*, v. 35, p. 331–34.

722   Laskar, J., Robutel, P., Joutel, F., Gastineau, M., Correia, A.C.M., Levrard, B., 2004. A long-term  
723           numerical solution for the insolation quantities of the Earth: *Astron. Astrophys*, v. 428 (1),  
724           p. 261–285.

725   Levy, R.H., Meyers, S.R., Naish, T.R., Golledge, N.R., McKay, R.M., Crampton, J.S., DeConto,  
726           R.M., De Santis, L., Florindo, F., Gasson, E.G.W., Harwood, D.M., Luyendyk, B.P.,  
727           Powell, R.D., Clowes, C., Kulhanek, D.K., 2019, Antarctic ice-sheet sensitivity to  
728           obliquity forcing enhanced through ocean connections: *Nature Geoscience*, v. 12, p.

729 132-137.

730 Li, M., Huang, C., Hinnov, L., Ogg, J., Chen, Z.-Q., Zhang, Y., 2016, Obliquity-forced climate  
731 during the Early Triassic hothouse in China: *Geology*, v. 44, p. 623-626.

732 Li, M., Hinnov, L.A., Huang, C., Ogg, J.G., 2018, Sedimentary noise and sea levels linked to  
733 land-ocean water exchange and obliquity forcing: *Nat Commun.*, v. 9, p. 1004.

734 Li, M., Hinnov, L., Kump, L., 2019a, Acycle: time-series analysis software for paleoclimate  
735 research and education: *Comput. Geosci.*, v. 127, p. 12-22.

736 Li, M., Huang, C., Ogg, J., Zhang, Y., Hinnov, L., Wu, H., Chen, Z.-Q., Zou, Z., 2019b,  
737 Paleoclimate proxies for cyclostratigraphy: Comparative analysis using a Lower Triassic  
738 marine section in South China: *Earth-Science Reviews*, v. 189, p. 125-146.

739 Li, Q., Yu, L. Z., Straub, K. M., 2016, Storage thresholds for relative sea-level signals in the  
740 stratigraphic record: *Geology*, v. 44, p. 179–82.

741 Li, X., Huang, Y., Zhang, Z., Wang, C., 2022, Chemical weathering characteristics of the Late  
742 Cretaceous Nenjiang Formation from the Songliao Basin (Northeastern China) reveal  
743 prominent Milankovitch band variations: *Palaeogeography, Palaeoclimatology,*  
744 *Palaeoecology*, v. 601, p. 111130.

745 Ma, C., Meyers, S.R., Sageman, B.B., 2017, Theory of chaotic orbital variations confirmed by  
746 Cretaceous geological evidence: *Nature*, v. 542, p. 468-470.

747 Ma, C., Meyers, S.R., Sageman, B.B., 2019, Testing Late Cretaceous astronomical solutions in a  
748 15 million year astrochronologic record from North America: *Earth and Planetary Science*  
749 *Letters*, v. 513, p. 1-11.

750 Ma, C., Li, M., 2020, Astronomical time scale of the Turonian constrained by multiple  
751 paleoclimate proxies: *Geoscience Frontiers*, v. 11, p. 1345-1352.

752 Mann, M.E., Lees, J.M., 1996, Robust estimation of background noise and signal detection in  
753 climatic time series: *Clim. Change*, v. 33, p. 409–445,  
754 <https://doi.org/10.1007/BF00142586>.

755 Mateo, P., Keller, G., Punekar, J., Spangenberg, J.E., 2017, Early to late Maastrichtian  
756 environmental changes in the Indian Ocean compared with Tethys and South Atlantic:  
757 *Paleogeogr. Paleoclimatol. Paleoecol.*, v. 478, p. 121–138,  
758 <https://doi.org/10.1016/j.palaeo.2017.01.027>.

759 Meyers, S. R and Sageman, B. B., 2007, Quantification of Deep-Time Orbital Forcing by Average  
760 Spectral Misfit: *American Journal of Science*, v. 307, p. 773-792.

761 Meyers, S. R., 2015, The evaluation of eccentricity-related amplitude modulation and bundling in  
762 paleoclimate data: An inverse approach for astrochronologic testing and time scale  
763 optimization: *Paleoceanography*, 30, doi:10.1002/2015PA002850.

764 Meyers, S. R., 2019, Cyclostratigraphy and the problem of astrochronologic testing: *Earth-Science*  
765 *Reviews*, v. 190, p. 190-223.

766 Meyers, S. R., 2014, Astrochron: An R package for astrochronology. [Available at [http://](http://cran.r-project.org/package=astrochron)  
767 [cran.r-project.org/package=astrochron](http://cran.r-project.org/package=astrochron).]

768 Meyers, S.R., Sageman, B.B., Arthur, M.A., 2012a, Obliquity forcing of organic matter  
769 accumulation during Oceanic Anoxic Event 2: *Paleoceanography*, v. 27, PA3212.  
770 <https://doi.org/10.1029/2012PA002286>.

771 Miller, K.G., Wright, J.D., Browning, J.V., 2005, Visions of ice sheets in a greenhouse world:  
772 *Mar. Geol.*, v. 217, p. 215–231, <https://doi.org/10.1016/j.margeo.2005.02.007>.

773 Olsen, P.E., Laskar, J., Kent, D.V., Kinney, S.T., Reynolds, D.J., Sha, J., Whiteside, J.H., 2019,  
774 Mapping Solar System chaos with the Geological Orrery: *PNAS*, v. 116, p. 10664-10673.

775 Opluštil, S., Laurin, J., Hýlová, L., Jirásek, J., Schmitz, M., Sivek, M., 2022, Coal-bearing fluvial  
776 cycles of the late Paleozoic tropics; astronomical control on sediment supply constrained  
777 by high-precision radioisotopic ages, Upper Silesian Basin: *Earth-Science Reviews*, v.  
778 228, p. 103998.

779 Raymo, M. E., Nisancioglu, K. H., 2003, The 41 kyr world: Milankovitch's other unsolved  
780 mystery: *Paleoceanogr. Paleoclimatol.*, v. 18, p. 1011.

781 Ripepe, M., Fischer, A. G., 1991, Stratigraphic rhythms synthesized from orbital variations: *J.*  
782 *Sediment. Petrol.*, v. 63, p. 335–344.

783 R Core Team, 2021, *R: A Language and Environment for Statistical Computing*: Vienna, Austria,  
784 R Foundation for Statistical Computing.

785 Sadler, P. M., and D. J. Strauss., 1990, Estimation of completeness of stratigraphical sections  
786 using empirical data and theoretical models: *J. Geol. Soc.*, v. 147, p. 471–485,  
787 doi:10.1144/gsjgs.147.3.0471.

788 Sinnesael, M., David De Vleeschouwer., Christian, Z., Anna Joy Drury, Gabriele Gambacortai,  
789 Frederik. Hilgenj, Linda A. Hinnov, Alexander J.L. Hudson, David B. Kemp, Margriet L.  
790 Lantink, Jiří Laurin, Mingsong Li, Diederik Liebrand, Chao Ma, Stephen R. Meyers,  
791 Johannes Monkenbusch, Alessandro Montanari, Theresa Nohl, Heiko Pälike, Damien Pas,  
792 Micha Ruhl, Nicolas Thibault, Maximilian Vahlenkamp, Luis Valero, Sébastien Wouters,  
793 Huaichun Wu, Philippe Claeys, 2019, The Cyclostratigraphy Intercomparison Project  
794 (CIP): consistency, merits and pitfalls: *Earth Science Reviews*, v. 199, p. 102965.

795 Sinnesael, M., Zivanovic, M., David De Vleeschouwer, and Philippe Claeys1., 2018, Spectral  
796 Moments in Cyclostratigraphy: Advantages and Disadvantages Compared to more Classic  
797 Approaches: *Paleoceanography and Paleoclimatology*, v. 33,

798 <https://doi.org/10.1029/2017PA00329>

799 Strasser, A., Hilgen, F.J., Heckel, P.H., 2006, Cyclostratigraphy – concepts, definitions, and  
800 applications: *Newsletters on Stratigraphy*, v. 42, p. 75-114.

801 Thomson, D.J., 1982, Spectrum estimation and harmonic analysis: *Proc. IEEE*, v. 70, p.  
802 1055–1096. <https://doi.org/10.1109/PROC.1982.12433>.

803 Torrence, C., Compo, G.P., 1998, A practical guide to wavelet analysis: *Bulletin of the American*  
804 *Meteorological Society*, v. 79, p. 61-78.

805 Valero, L., Garcés, M., Cabrera, L., Costa, E., Sáez, A., 2014, 20 Myr of eccentricity paced  
806 lacustrine cycles in the Cenozoic Ebro Basin: *Earth and Planetary Science Letters*, v. 408,  
807 p. 183-193.

808 Walters, A. P., Carroll, A. R., Meyers, S. R., and Lowenstein, T. K., 2023, Influence of lake-basin  
809 morphology on climate-sediment transfer functions: Early Eocene Wilkins Peak Member,  
810 Green River Formation, Wyoming: *GSA Bulletin*, <https://doi.org/10.1130/B36566.1>

811 Wan, X., Zhao, J., Scott, R.W., Wang, P., Feng, Z., Huang, Q., Xi, D., 2013, Late Cretaceous  
812 stratigraphy, Songliao Basin, NE China: SK1 cores: *Paleogeogr. Paleoclimatol. Paleoecol.*,  
813 v. 385, p. 31–43, <https://doi.org/10.1016/j.palaeo.2012.10.024>.

814 Wang, C., Feng, Z., Zhang, L., Huang, Y., Cao, K., Wang, P., Zhao, B., 2013, Cretaceous  
815 paleogeography and paleoclimate and the setting of SKI borehole sites in Songliao Basin,  
816 Northeast China: *Paleogeogr. Paleoclimatol. Paleoecol.*, v. 385, p. 17–30,  
817 <https://doi.org/10.1016/j.palaeo.2012.01.030>.

818 Wang, L., Song, Z., Cao, X., Li, Y., 2015, Compound-specific carbon isotope study on the  
819 hydrocarbon biomarkers in lacustrine source rocks from Songliao Basin: *Organic*  
820 *Geochemistry*, v. 87, p. 68-77.

821 Wang, M., Chen, H., Huang, C., Kemp, D.B., Xu, T., Zhang, H., Li, M., 2020, Astronomical  
822 forcing and sedimentary noise modeling of lake-level changes in the Paleogene Dongpu  
823 Depression of North China: *Earth and Planetary Science Letters*, v. 535, p. 116116.

824 Wang, T. T, Ramezani, J, Wang, C. S, Wu, H. C, He, H, Bowring, S. A., 2016, High-precision  
825 U–Pb geochronologic constraints on the Late Cretaceous terrestrial cyclostratigraphy and  
826 geomagnetic polarity from the Songliao Basin, Northeast China: *Earth Planet. Sci. Lett.*, v.  
827 446, p. 37–44.

828 Wang, Y., Baars, T.F., Storms, J.E.A., Martinius, A.W., Gingerich, P.D., Chmielewska, M.,  
829 Buckley, S.J., Abels, H.A., 2023. Lateral and vertical characteristics of floodplain  
830 aggradation cycles in the lower Eocene Willwood Formation, Bighorn Basin, Wyoming,  
831 USA: *GSA Bulletin*, doi: <https://doi.org/10.1130/B36908.1>.

832 Wang, Z., Huang, C., Kemp, D.B., Zhang, Z., Sui, Y., 2021, Distinct responses of late Miocene  
833 eolian and lacustrine systems to astronomical forcing in NE Tibet, *GSA Bulletin*, v. 133  
834 (11-12), p. 2266–2278, doi: <https://doi.org/10.1130/B35776.1>.

835 Wei, R., Li, M., Zhang, R., Hu, Y., James Ogg, Liu, G., Huang, H., He, X., Yuan, S., Lin, Q., Jin,  
836 Z., 2023. Obliquity forcing of continental aquifers during the late Paleozoic ice age: *Earth  
837 and Planetary Science Letters*, v. 613, 118174.

838 Westerhold, T., Marwan, N., Drury, A.J., Diederik Liebrand, Claudia Agnini, Eleni Anagnostou,  
839 James S. K. Barnet, Steven M. Bohaty, David De Vleeschouwer, Fabio Florindo, Thomas  
840 Frederichs, David A. Hodell, Ann E. Holbourn, Dick Kroon, Vittoria Lauretano, Kate  
841 Littler, Lucas J. Lourens, Mitchell Lyle, Heiko Pälike, Ursula Röhl, Jun Tian, Roy H.  
842 Wilkens, Paul A. Wilson, James C. Zachos, 2020, An astronomically dated record of  
843 Earth’s climate and its predictability over the last 66 million years: *Science*, v. 369, p.

844 1383-1387.

845 Westphal, H., Böhm, F., and Bornholdt, S., 2004, Orbital frequencies in the carbonate sedimentary  
846 record—Distorted by diagenesis?: *Facies*, v. 50, p. 3–11, doi:  
847 10.1007/s10347-004-0005-x.

848 Wouters, S., Crucifix, M., Sinnesael, M., Da Silva, A. C., Zeeden, C., Zivanovic, M., Boulvain, F.,  
849 Devleeschouwer, X., 2022, A decomposition approach to cyclostratigraphic signal  
850 processing: *Earth-Science Reviews*, v. 225, p. 103894.

851 Wu, H., Zhang, S., Jiang, G., Hinnov, L., Yang, T., Li, H., Wan, X., Wang, C., 2013,  
852 Astrochronology of the Early Turonian–Early Campanian terrestrial succession in the  
853 Songliao Basin, northeastern China and its implication for long-period behavior of the  
854 solar system: *Palaeogeogr. Palaeoclimatol. Palaeoecol.*, v. 385, p. 55–70.

855 Wu, H., Zhang, S., Hinnov, L.A., Jiang, G., Yang, T., Li, H., Wan, X., Wang, C., 2014,  
856 Cyclostratigraphy and orbital tuning of the terrestrial upper Santonian–lower Danian in  
857 Songliao Basin, northeastern China: *Earth Planet. Sci. Lett.*, v. 407, p. 82–95.  
858 <https://doi.org/10.1016/j.epsl.2014.09.038>.

859 Wu, H., Hinnov, L.A., Zhang, S., Jiang, G., Yang, T., Li, H., Xi, D., Ma, X., Wang, C., 2022,  
860 Continental geological evidence for Solar System chaotic behavior in the Late Cretaceous:  
861 *GSA Bulletin*, v. 135, P. 712-724, <https://doi.org/10.1130/B36340.1>.

862 Zeebe, R. E and Lourens, L. J., 2019, Solar System chaos and the Paleocene–Eocene boundary age  
863 constrained by geology and astronomy: *Science*, v. 365, p. 926-929.